

# DEVELOPMENT OF A LASER-BASED SYSTEM FOR THE DETECTION OF FLAWS IN SOLID ROCKET MOTORS

J.L. Doyle  
R. McCullough  
G.K. Torrington

QUEST Integrated, Inc.  
21414 68th Ave. S.  
Kent, WA 98032

May 1996

## Final Report

Distribution authorized to DoD components only; Proprietary Information; May 1996. Other requests for this document shall be referred to AFMC/STI.

**WARNING** - This document contains technical data whose export is restricted by the Arms Export Control Act (Title 22, U.S.C., Sec 2751 et seq.) or The Export Administration Act of 1979, as amended (Title 50, U.S.C., App. 2401, et seq.). Violations of these export laws are subject to severe criminal penalties. Disseminate IAW the provisions of DoD Directive 5230.25 and AFI 61-204.

**DESTRUCTION NOTICE** - For classified documents, follow the procedures in DoD 5200.22-M, Industrial Security Manual, Section II-19 or DoD 5200.1-R, Information Security Program Regulation, Chapter IX. For unclassified, limited documents, destroy by any method that will prevent disclosure of contents or reconstruction of the document.

19960802 000



**PHILLIPS LABORATORY**  
Space and Missiles Technology Directorate  
AIR FORCE MATERIEL COMMAND  
KIRTLAND AIR FORCE BASE, NM 87117-5776

UNCLASSIFIED



AD NUMBER

AD-B213 297

NEW LIMITATION CHANGE

TO

DISTRIBUTION STATEMENT A -  
Approved for public release; Distri-  
bution unlimited.

Limitation Code: 1

FROM

DISTRIBUTION STATEMENT -

Limitation Code:

AUTHORITY

Janet E. Mosher; Phillips Lab/CA, Kirtland AFB,  
N.M.

THIS PAGE IS UNCLASSIFIED

PL-TR-96-1016

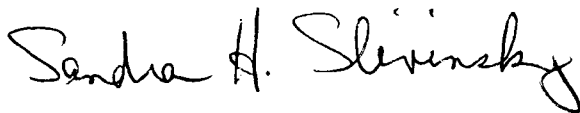
Using Government drawings, specifications, or other data included in this document for any purpose other than Government procurement does not in any way obligate the U.S. Government. The fact that the Government formulated or supplied the drawings, specifications, or other data, does not license the holder or any other person or corporation; or convey any rights or permission to manufacture, use, or sell any patented invention that may relate to them.

This report contains proprietary information and shall not be either released outside the government, or used, duplicated or disclosed in whole or in part for manufacture or procurement, without the written permission of the contractor. This legend shall be marked on any reproduction hereof in whole or in part.

If you change your address, wish to be removed from this mailing list, or your organization no longer employs the addressee, please notify PL/VT-B, 3550 Aberdeen Ave SE, Kirtland AFB, NM 87117-5776.

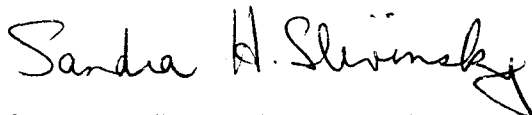
Do not return copies of this report unless contractual obligations or notice on a specific document requires its return.

This report has been approved for publication.



SANDRA SLIVINSKY, GM-14  
Project Manager

FOR THE COMMANDER



SANDRA SLIVINSKY, GM-14  
Chief, Ballistic Missiles Technology  
Program Office



HENRY L. PUGH, JR., Col, USAF  
Director, Space and Missiles Technology  
Directorate

The following notice applies to any unclassified (including originally classified and now declassified) technical reports released to "qualified U.S. contractors" under the provisions of DoD Directive 5230.25, Withholding of Unclassified Technical Data From Public Disclosure.

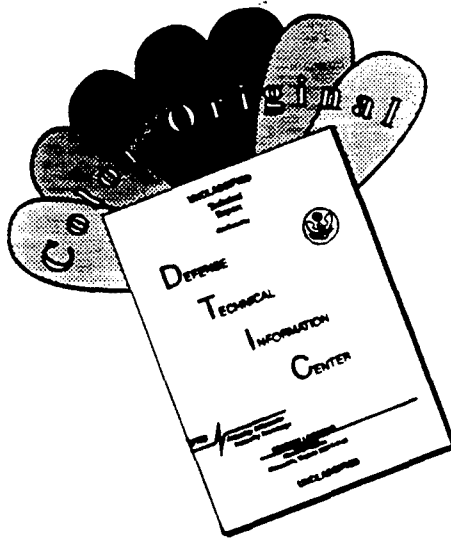
NOTICE TO ACCOMPANY THE DISSEMINATION OF EXPORT-CONTROLLED TECHNICAL DATA

1. Export of information contained herein, which includes, in some circumstances, release to foreign nationals within the United States, without first obtaining approval or license from the Department of State for items controlled by the International Traffic in Arms Regulations (ITAR), or the Department of Commerce for items controlled by the Export Administration Regulations (EAR), may constitute a violation of law.
2. Under 22 U.S.C. 2778 the penalty for unlawful export of items or information controlled under the ITAR is up to two years imprisonment, or a fine of \$100,000, or both. Under 50 U.S.C., Appendix 2410, the penalty for unlawful export of items or information controlled under the EAR is a fine of up to \$1,000,000, or five times the value of the exports, whichever is greater; or for an individual, imprisonment of up to 10 years, or a fine of up to \$250,000, or both.
3. In accordance with your certification that establishes you as a "qualified U.S. Contractor", unauthorized dissemination of this information is prohibited and may result in disqualification as a qualified U.S. contractor, and may be considered in determining your eligibility for future contracts with the Department of Defense.
4. The U.S. Government assumes no liability for direct patent infringement, or contributory patent infringement or misuse of technical data.
5. The U.S. Government does not warrant the adequacy, accuracy, currency, or completeness of the technical data.
6. The U.S. Government assumes no liability for loss, damage, or injury resulting from manufacture or use for any purpose of any product, article, system, or material involving reliance upon any or all technical data furnished in response to the request for technical data.
7. If the technical data furnished by the Government will be used for commercial manufacturing or other profit potential, a license for such use may be necessary. Any payments made in support of the request for data do not include or involve any license rights.
8. A copy of this notice shall be provided with any partial or complete reproduction of these data that are provided to qualified U.S. contractors.

D E S T R U C T I O N      N O T I C E

For classified documents, follow the procedures in DoD 5200.22-M, Industrial Security Manual, Section II-19 or DoD 5200.1-R, Information Security Program Regulation, Chapter IX. For unclassified, limited documents, destroy by any method that will prevent disclosure of contents or reconstruction of the document.

# DISCLAIMER NOTICE



THIS DOCUMENT IS BEST QUALITY AVAILABLE. THE COPY FURNISHED TO DTIC CONTAINED A SIGNIFICANT NUMBER OF COLOR PAGES WHICH DO NOT REPRODUCE LEGIBLY ON BLACK AND WHITE MICROFICHE.

# DRAFT SF 298

<b>1. Report Date (dd-mm-yy)</b> May 1996		<b>2. Report Type</b> Final		<b>3. Dates covered (from... to )</b> 04/94 to 03/95		
<b>4. Title &amp; subtitle</b> Development of a Laser-Based System for the Detection of Flaws in Solid Rocket Motors			<b>5a. Contract or Grant #</b> F29601-94-C-0084			
			<b>5b. Program Element #</b> 62601F			
<b>6. Author(s)</b> J.L. Doyle R. McCullough G.K. Torrington			<b>5c. Project #</b> 3005			
			<b>5d. Task #</b> CO			
			<b>5e. Work Unit #</b> GS			
<b>7. Performing Organization Name &amp; Address</b> QUEST Integrated, Inc. 21414 68th Ave. S. Kent, WA 98032				<b>8. Performing Organization Report #</b>  658		
<b>9. Sponsoring/Monitoring Agency Name &amp; Address</b> Phillips Laboratory 3550 Aberdeen Ave SE Kirtland AFB, NM 87117-5776				<b>10. Monitor Acronym</b>		
				<b>11. Monitor Report #</b> PL-TR-96-1016		
<b>12. Distribution/Availability Statement</b> Distribution authorized to DoD components only; Proprietary Information: May 1996. Other requests for this document shall be referred to AFMC/STI.						
<b>13. Supplementary Notes</b>						
<b>14. Abstract</b> Solid rocket motors are often stored for long periods of time, frequently under extreme environmental conditions. Thermal cycling and aging can induce internal flaws, such as cracking and slumping, that can lead to catastrophic failures, often resulting in significant loss of property and even loss of life. This report summarizes the results of the Phase I study to develop a lightweight, portable, and rugged system that is capable of conducting automated inspections of solid rocket motors for these types of internal flaws. The Solid Rocket Motor Inspection System will employ noncontacting, low-power, laser-based sensor technology to rapidly obtain accurate and quantitative data that is then generated into a three-dimensional map of the motor inside surfaces. The fundamental system design is based on a field-proven, laser-based inspection technology that has been used in similar systems delivered to the U.S. Army, Navy, and Air Force. The resulting remote inspection system provides a cost-effective solution to current inspection problems and has direct extensions to commercial nondestructive evaluation applications.						
<b>15. Subject Terms</b> Laser, Triangulation, Flaws, Solid Rocket Motors, Nondestructive Testing, Cracks						
<b>Security Classification of</b>				<b>19. Limitation of Abstract</b>  Limited	<b>20. # of Pages</b>  68	<b>21. Responsible Person (Name and Telephone #)</b>  Sandra Slivinsky (505) 846-5799
<b>16. Report unclassified</b>	<b>17. Abstract unclassified</b>	<b>18. This Page unclassified</b>				

## SBIR RIGHTS NOTICE

These SBIR data are furnished with SBIR rights under Contract No. F29601-94-C-0084. For a period of 4 years after acceptance of all times to be delivered under this contract, the Government agrees to use these data for Government purposes only, and they shall not be disclosed outside the Government (including disclosure for procurement purposes) during such period without permission of the Contractor, except that, subject to the foregoing use and disclosure prohibitions, such data may be disclosed for use by support Contractors. After the aforesaid 4-year period the Government has a royalty-free license to use, and to authorize others to use on its behalf, these data for Government purposes, but is relieved of all disclosure prohibitions and assumes no liability for unauthorized use of these data by third parties. This Notice shall be affixed to any reproductions of these data, in whole or in part.

## PREFACE AND ACKNOWLEDGMENTS

The following report summarizes the work conducted under the Department of Defense Contract No. F29601-94-C-0084 under the auspices of Phillips Laboratory, Directorate of Space Technologies, Air Force Systems Command, Kirtland Air Force Base, New Mexico.

The authors wish to express special appreciation for the support provided by Dr. Sandra Slivinsky of Phillips Laboratory.



# CONTENTS

<u>Section</u>	<u>Page</u>
Report Documentation Page .....	i
SBIR Rights Notice.....	ii
Preface and Acknowledgments.....	iii
Figures.....	v
Summary .....	1
2. Background .....	2
2.1 SRM Principles of Operation .....	2
2.2 SRM Failure Modes .....	4
2.3 Noncontact Surface Profilometry by Optical Triangulation.....	5
3. Objective of Phase I Research.....	8
4. Laboratory Work.....	9
4.1 Development of Test Specimens.....	9
4.1.1 Material Characterization .....	9
4.1.2 Building Test Specimens .....	12
4.2 Method of Evaluation.....	15
4.2.1 Laboratory Setup.....	15
4.2.2 Analysis Facilities.....	19
4.3 Test Results .....	23
4.3.1 Small Model .....	23
4.3.2 Large Model.....	31
5. Phase II Program Description .....	39
5.1 Phase II Technical Objectives .....	39
5.2 Preliminary Design.....	39
5.2.1 Sensor Assembly .....	41
5.2.2 Delivery System.....	46
5.2.3 Data Acquisition and Display System .....	47
5.2.4 Design Review.....	47
5.3 Summary of Phase I Results.....	48
5.3.1 Task 1 - Select Test Case.....	48
5.3.2 Task 2 - Select Optimum Sensor Configuration.....	48
5.3.3 Task 3 - Build Laboratory Test Setup.....	48
5.3.4 Task 4 - Conduct Laboratory Tests.....	49
5.3.5 Task 5 - Assimilate Results and Define Conceptual Inspection System .....	49
6. Summary and Conclusions.....	50
7. Recommendations.....	51
Appendix. MATLAB Scripts for Analysis and Display .....	52

## FIGURES

<u>Figure</u>		<u>Page</u>
1.	Basic components of a solid rocket motor.	3
2.	Operational principle of optical triangulation.	6
3.	Lateral-effect photodetector.	7
4.	Material characterization experimental setup.	10
5.	Surface profile of inert propellant grain sample.	10
6.	Photograph of material characterization experiment.	11
7.	Self-correlation analysis of surface profile data from the inert propellant grain sample.	12
8.	Surface profile of Sculptey™ II modeling clay.	13
9.	Self-correlation analysis of surface profile data from the Sculptey™ II modeling clay sample.	13
10.	Template for small-model cutting tool.	14
11.	Template for large-model cutting tool.	14
12.	Diagram of experimental setup.	15
13.	Photograph of experimental setup.	16
14.	Assembly drawing of in-house optical triangulation head.	17
15.	Calibration curve of the in-house probe.	18
16.	Full fin scan of Sample #2.	21
17.	Simulated full bore scan of Sample #1.	24
18.	Photograph of Sample #1.	25
19.	Full fin scan of Sample #1.	26
20.	Photographs of crack in Sample #2.	27

## FIGURES (Continued)

<u>Figure</u>		<u>Page</u>
21.	High-density scan of Sample #2 in neighborhood of crack.	28
22.	Photograph of crack in Sample #3.	29
23.	High-density scan of Sample #3 in neighborhood of crack.	30
24.	Photograph of Sample #2 with surface deviated flaw detection.	31
25.	Scan of Sample #2 with surface deviation flaw detection.	32
26.	Scan of Sample #2 with reflected intensity deviation flaw detection.	33
27.	Scan of flawless large-model sample.	34
28.	Simulated full-bore scan.	35
29.	Photograph of large-model sample.	36
30.	Scan of crack on large-model sample.	37
31.	Photograph of crack present of large-model sample.	38
32.	Conceptual view of Solid Rocket Motor Inspection System.	40
33.	Sensor assembly.	41
34.	Photo of GrIn lens attached to optical fiber.	42
35.	Laser-Optic Tube Inspection System.	43
36.	LOTIS probes.	44
37.	Rotating LOTIS sensor.	44
38.	The results of automated, laser-based scanning displayed in summary, isometric, and cross-sectional perspectives.	45
39.	Delivery system.	46
40.	Block diagram of SRMIS Data Acquisition and Display System.	47

## 1. SUMMARY

Solid rocket motors (SRMs) are found in a wide variety of military and aerospace vehicles. The basic propellant technology behind SRMs has a variety of nonpropulsion applications such as in the use of compact pressure generation devices and in the gas supply for air bags in cars. They are extremely simple; they have no moving parts, and they do not require storing a volatile and often hazardous liquid, which may also be a cryogenic. This simplicity results in the highly reliable operation of SRMs; although failures do occur, often with spectacular results due to the availability of the complete fuel mass within a single volume.

The objective under Phase I was to determine the feasibility of inspecting the interior surfaces of SRMs using laser-based triangulation methods. A performance specification was developed and formed the foundation of a preliminary design for the system. This design considered the range of SRM internal geometries and surface properties. Also considered was the instrument's capability of measuring surface roughness and reflectivity. Possible techniques for establishing surface composition were investigated.

The Phase I technical approach builds on QUEST's considerable experience by adapting our field-proven laser-based profilometry technology to this application. We conducted a literature survey and worked with the technical monitor to determine propellants of greatest interest on the inventory and their chemical and spectral properties. The results will be used in Phase II to design and build a prototype of an accurate, portable, and cost-effective inspection system that will be capable of mapping the dimensions and surface characteristics found in SRMs.

Phase I was conducted on a task-by-task basis. A test case for the interior surface profile for a relatively difficult "star" cross section of the motor was agreed upon. Understanding the behavior of laser-based triangulation sensors in this application was achieved by laboratory testing. Various types of cracking and slumping flaws were simulated in the modeling clay that was then fired and placed into mounts for scanning. It was clearly demonstrated that small changes in surface reflectivity or surface shape could be detected due to the presence of droplets on the surface.

It is recommended that the Phase II program be carried out. The objective will be to develop a lightweight, portable, and rugged system capable of conducting automated inspections of SRMs. Specific technical objectives include (1) developing a detailed system specification that will address functional, environmental, and safety requirements for the system; (2) developing a system design that will meet the inspection needs of the U.S. Air Force and its civilian suppliers; (3) demonstrating a prototype SRM Inspection System (SRMIS) in the laboratory and under field conditions; and (4) conducting a preliminary market study for a Phase III commercialization program.

## 2. BACKGROUND

Solid rocket motors (SRM's) are found in a wide variety of military and aerospace vehicles. In military applications, they are used in tactical missiles (e.g., air-to-air Sidewinder and shoulder-launched Stinger) and intercontinental ballistic missiles, such as Minuteman. In space applications, SRM's also have a wide variety of uses, from small sounding rockets to orbital assist modules to the large solid rocket boosters associated with the space shuttle program. In addition, the basic propellant technology behind SRM's has a variety of nonpropulsion applications such as the use as compact pressure generation devices and as the gas supply for air bags in cars.

In contrast to liquid rocket motors, solid propellant motors are extremely simple; they have no moving parts. In addition, they do not have the requirement of storing a volatile and often hazardous liquid, which may also be a cryogenic. The absence of moving parts and the inherent simplicity in SRM's make them ideal for applications in which the motor must be stored for extended periods of time before use. This simplicity results in the highly reliable operation of SRM's; although failures do occur, often with spectacular results due to the availability of the complete fuel mass within a single volume.

### 2.1 SRM PRINCIPLES OF OPERATION

The basic components of an SRM are shown in Figure 1. The motor consists of a case that acts as a pressure containment vessel and a nozzle for directing the flow and generating the thrust. The case contains the solid rocket propellant, forming a "grain". Between the propellant and the case, there is a layer of liner, then the insulation. The function of the insulation is to serve as a thermal barrier between the propellant and the case, as the hot products of combustion of the solid propellant are generated after motor ignition. The liner material serves to provide an effective bond between the propellant material and the insulation. Although the configuration of the SRM appears to be simple, a substantial design and engineering effort is required for the successful production of the motor. The casing material, for weight savings, is often fabricated from an advanced composite material, and the propellant is a viscoelastic material. The SRM's are subjected to a wide variety of stresses, including those incurred during long-term storage, transportation forces, and shock forces during use. The design of an SRM is a complex task involving tradeoffs between propulsion performance, service life, and reliability.

In general, a rocket motor functions by generating high-pressure gases during combustion. These gases expand through a nozzle under supersonic conditions, providing the thrust required

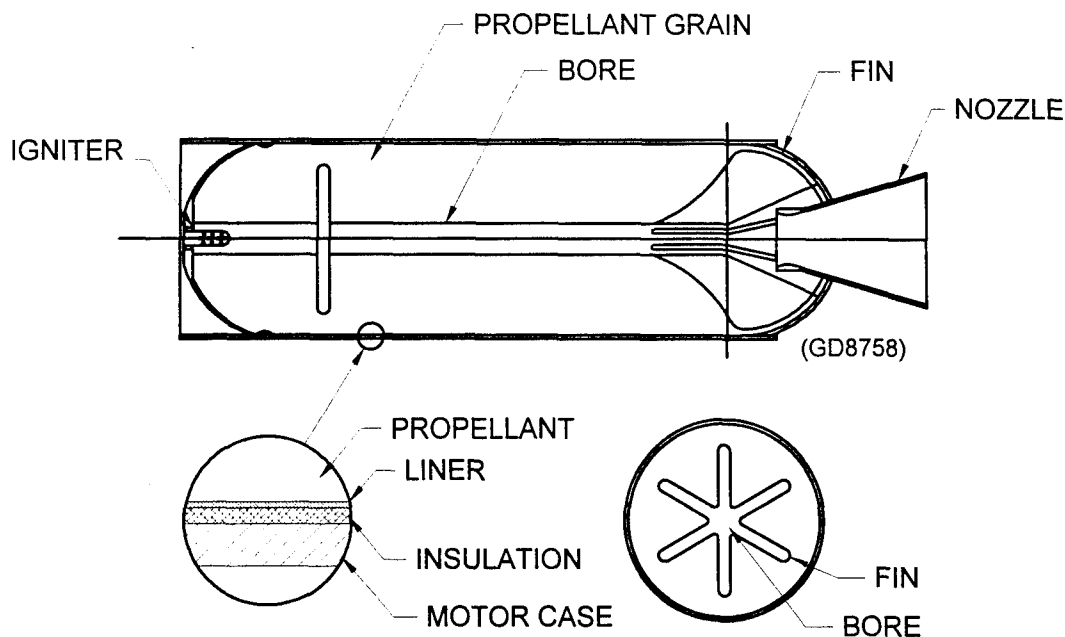


Figure 1. Basic components of a solid rocket motor.

of the SRM. In the case of solid propellant, the propellant surface burns in a controlled manner (not detonation). The surface burning rate or regression rate,  $r$ , measured in meters per second, exhibits a power law dependence with ambient pressure,  $p$ , given by

$$r = bp^n \quad (1)$$

where  $b$  and  $n$  are constants. For propulsion to be stable within the rocket motor, the exponent  $n$  generally has a value of less than 1. At any instant of time, the mass generation rate of propellant gases is then proportional to the surface area,  $S$ , of the propellant times the propellant density,  $\rho$ , times the burning rate,  $r$ , or

$$m = Spr \quad (2)$$

where  $m$  is the mass rate. These hot gases exit through a nozzle. The mass flowing through the nozzle is proportional to the nozzle throat area,  $A_t$ , and the pressure generated during combustion. The proportionality constant is a so-called discharge coefficient,  $C_d$ ; therefore, the mass flow of the nozzle is given by

$$m = C_d A_t p \quad (3)$$

During ignition the pressure in the combustion chamber rises until an equilibrium is established in which the mass generated by combustion of the propellant surface is balanced by the flow of gases through the nozzle. Solving for pressure from Equations (1) through (3), we arrive at the expression

$$p = \left( \frac{S \rho b}{A_t C_d} \right)^{\frac{1}{1-n}} \quad (4)$$

We see from Equation (4) that for typical values of the burning exponent,  $n$ , of 0.7 to 0.8, the exponent on the right-hand side can be on the order of 3 to 4. This is a very sensitive dependence upon the parameters inside the expression. With these values, the sensitivity to pressure in the cases is extremely high. Unplanned increases in the surface area or decreasing throat area ( $A_t$ ) will therefore result in a high pressure due to the large exponent of the expression in parenthesis.

## 2.2 SRM FAILURE MODES

Specific data on failure modes in SRM's are difficult to obtain due to the explosive nature of the failure. In events in which motor fragments have been recovered following a failure, several probable causes for motor failure have been identified. These causes include cracking of the motor grain, slumping of the motor grain, chemical compositional change of the motor grain, failure of the bonding between the grain, liner, and insulator or the insulator and the case, and failure of the case or nozzle. It was the purpose of our Phase I research program to evaluate laser optical profilometry for the detection of faults that can indicate probable failure in rocket motors.

If we examine the individual terms that make up the right-hand side of Equation (4), we see that in the numerator is the surface area of the propellant. Thus, if the surface area increases during burning from unexpected causes, the pressure in the motor can rise rapidly to catastrophic levels. Two major causes for the surface area increase that have been identified in the past are the presence of cracking in the motor grain and disbonds between the propellant and liner. In the former case, the cracking occurs at the surface, allowing combustion gases to enter the body of the propellant and ignite the additional surface area. For the case of disbonding between the propellant and the liner, the propellant burns in areas not designed to be burned, thereby also increasing the surface area.

We also see by Equation (4) that the nozzle parameters can affect the pressure in the chamber as well. Another cause of rocket motor failure has been identified as slumping of the propellant. This occurs due to the viscoelastic nature of the propellant material. When stored for long times

at high temperatures, the material can sag or slump. If this migration of propellant changes the flow characteristics of the nozzle by blockage or alteration of the flowfield near the nozzle, a change in the effective nozzle area or combustion pressure can occur. In addition, it has been speculated that some rocket motor failures have been caused by cracking and breaking off of large chunks of the propellant, thus blocking the nozzle and dramatically reducing the effective nozzle area.

Two other common modes of rocket failure can occur; these are caused by separation between the insulation and the motor case and decomposition of the propellant. In the former case, when the bonding between the insulation and the motor case fails, hot gases from the combustion portion can enter the region adjacent to the motor case. This causes an elevation in temperature and corresponding reductions in the mechanical properties of the motor case, thereby weakening it and causing failure. In the case of propellant decomposition, the failure is caused by a change in the chemical composition of the propellant. Such changes can cause a change in the burn rate, again leading to a disastrous increase in pressure.

### 2.3 NONCONTACT SURFACE PROFILOMETRY BY OPTICAL TRIANGULATION

QUEST Integrated, Inc., has developed a family of instruments that provide the capability of measuring interior dimensions of cavities to high accuracies. These instruments have been developed and fielded in several military applications and applied to problems as diverse as inspecting the insides of naval boiler tubes in ship propulsion systems to the interior surfaces of 120-mm gun barrels. These systems are based on laser triangulation and provide the ability to map the interior surface profile to accuracies of better than 0.025 mm. The focus of the effort under the Phase I and the proposed Phase II effort is to extend this technology to the nondestructive inspection of SRM interiors with the intent to detect surface flaws with the potential for causing failure. We believe that, of the flaws discussed above, the presence of cracking or dimensional changes due to sagging or slumping can be detected with a high degree of probability. This technology may not be capable of detecting debonds, although other techniques, such as shearography, for detecting very slight changes in the surface profile may hold promise in that area.

To apply the principle of optical triangulation, a small beam of light is projected at near-normal incidence onto the target surface (Figure 2). Receiving optics image this spot of light onto a single-axis, lateral-effect photodetector. Because the transmitting and receiving optics are positioned at different angles, changes in target proximity are converted to lateral movement on



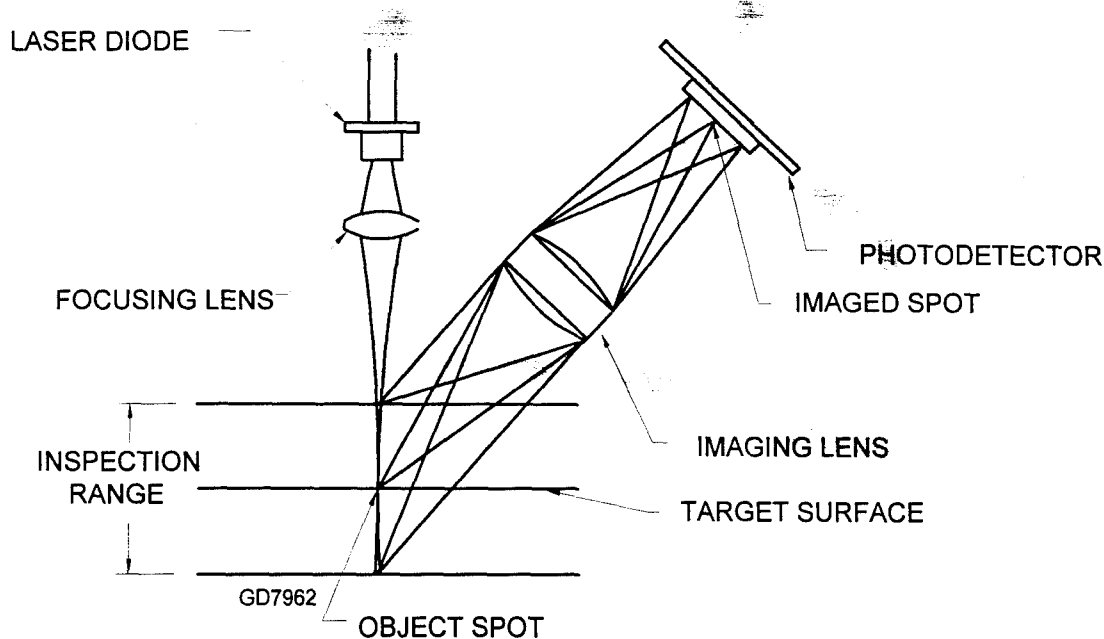


Figure 2. Operational principle of optical triangulation.

the photodetector. For a perfect optical system, the displacement of the light spot imaged on the detector is proportional to the position of the target.

Operation of the lateral-effect photodetector is straightforward. When light strikes this device (Figure 3), photocurrents flow to the anodes at the ends of the detector. These currents are proportional to the position and intensity of the imaged light spot. The magnitude of the photocurrents varies linearly as the position of the light changes on the photodetector. The position of the imaged spot,  $x$ , relative to the center of the photodetector is given by:

$$x = a (I_1 - I_2) / (I_1 + I_2) \quad (5)$$

where  $I_1$  and  $I_2$  are the two photocurrents, and  $a$  is a scale factor. By dividing the difference ( $I_1 - I_2$ ) by the sum ( $I_1 + I_2$ ), the effects of variations in received light intensity due to changes in reflectivity are reduced.

Calibrating the system for nonlinearities due to optical orientation, detector, offsets in the amplifier electronics, and reflectivity variations in the material results in precise radius measurements of the inside surface of the tube at each sample point. The system will sample several thousand data points during an inspection; therefore, a detailed map of the inside surface of a cavity can be generated.

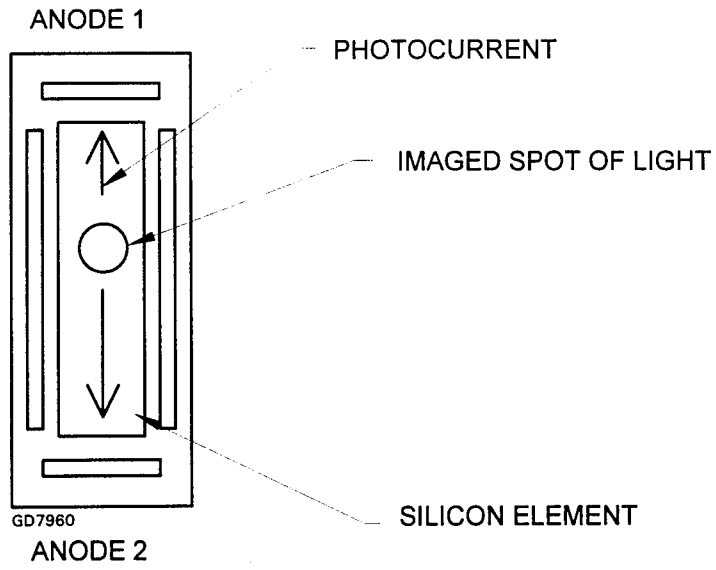


Figure 3. Lateral-effect photodetector.

### 3. OBJECTIVE OF PHASE I RESEARCH

Our objectives under Phase I were to determine the feasibility of inspecting the interior surfaces of SRM's using laser-based triangulation methods. A performance specification was developed and formed the foundation of a preliminary design for the system. This design considered the range of SRM internal geometries and surface properties. In addition, we investigated the ability of the instrument to measure surface roughness and reflectivity and reviewed possible techniques for establishing surface composition.

The following questions were addressed under Phase I:

- What accuracy and resolution can be expected in a laser optical triangulation inspection system for internal rocket motors using state-of-the-art laser sources and detectors?
- What are the fundamental system configuration requirements such as size, weight, and portability?
- What are the explosion-proofing requirements for the various types of propellants?
- In addition to surface dimensionality, what surface-related variables will be of interest to SRM quality control personnel? These may include roughness, reflectivity, and chemical composition.

The technical approach of Phase I was to build on our considerable experience by adapting our field-proven laser-based profilometry technology to this application. We conducted a literature survey and worked with the technical monitor to determine propellants of greatest interest in the inventory and their chemical and spectral properties. The results will be used in Phase II to design and build a prototype of an accurate, portable, and cost-effective inspection system that will be capable of mapping the dimensions and surface characteristics found in composite propellants.

The Phase I program was divided into six tasks as listed below:

- Task 1 - Select Test Case
- Task 2 - Select Optimum Sensor Configuration
- Task 3 - Build Laboratory Test Setup
- Task 4 - Conduct Laboratory Tests
- Task 5 - Assimilate Results and Define Conceptual Inspection System
- Task 6 - Write Final Report

## 4. LABORATORY WORK

### 4.1 DEVELOPMENT OF TEST SPECIMENS

The first order of business was to create a representative sample of an SRM grain. QUEST was provided an inert sample of simulated propellant and a description of typical SRM geometries that exist in the U.S. arsenal. Using this information, a series of samples was made based on two different geometries exhibiting different types of defects. Two sizes of samples were created in order to have suitable test beds for the two triangulation sensors employed in testing. The following sections detail this effort.

#### 4.1.1 Material Characterization

In the proposed optical triangulation sensor, the key material property is the surface reflectivity of near-infrared radiation. Our goal was to identify a material that would be easy to shape and would exhibit similar surface reflectivity to the propellant sample.

The experimental setup is diagrammed in Figure 4. QUEST employed a Keyence LC-2100 Laser Displacement Sensor to measure surface reflectivity. This device is a commercially available optical triangulation sensor employing a semiconductor laser diode with 670-nm wavelength output. In addition to displacement, the sensor is also capable of measuring the total reflected light signal. The LC-2100 outputs an analog signal proportional to the measured quantity (displacement or reflected intensity) that we recorded using a standard 486 computer with a DAS-8 analog data acquisition board. The sensor was mounted on an four-axis robot and scanned across the surface of the sample. Data from these scans could then be compared for different samples in order to assess reflectivity.

The sample SRM grain was light gray in color and slightly ductile, surprisingly similar to standard modeling clay. Therefore, we used Sculptey™ II modeling clay as our test specimen.

Inert Propellant Sample. Data from a scan of the inert propellant sample are presented in Figure 5. This scan was taken over the flat top region of the grain sample. Abscissa values represent scaled reflected radiance from the Keyence LC-2100. A photograph of this arrangement is shown in Figure 6. The laser is projected at normal incidence in this case. We observed an average value of 0.068 (in Keyence-defined units).

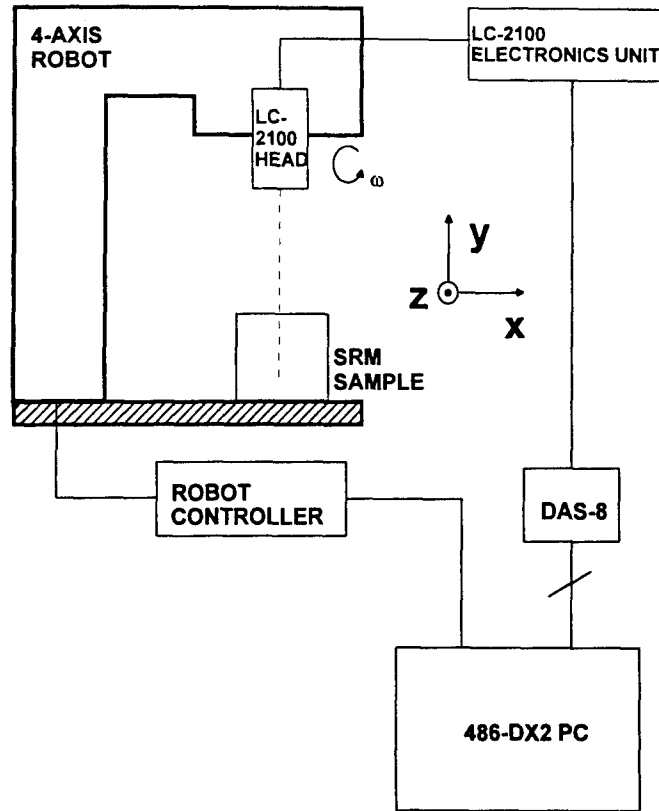


Figure 4. Material characterization experimental setup.

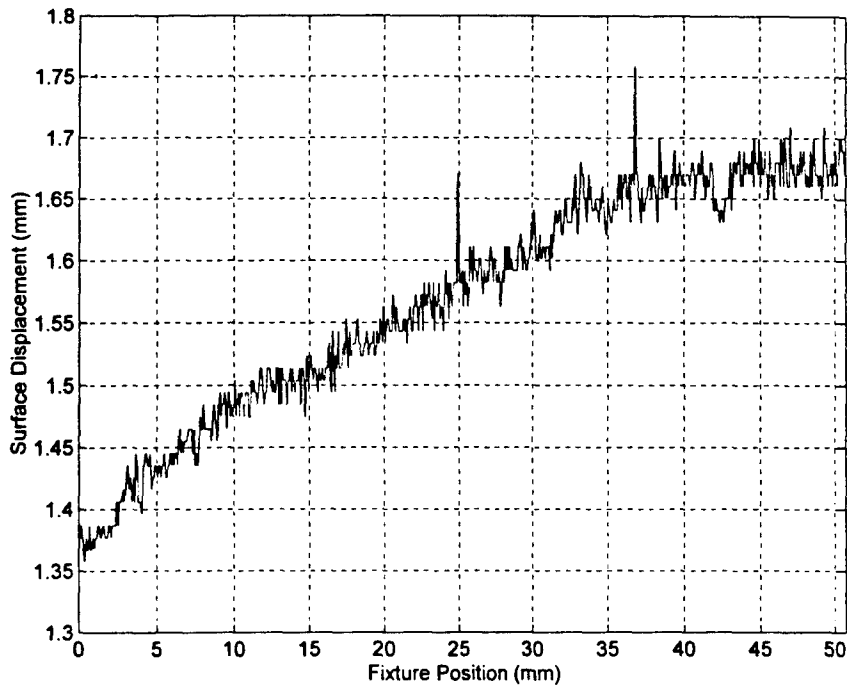


Figure 5. Surface profile of inert propellant grain sample.

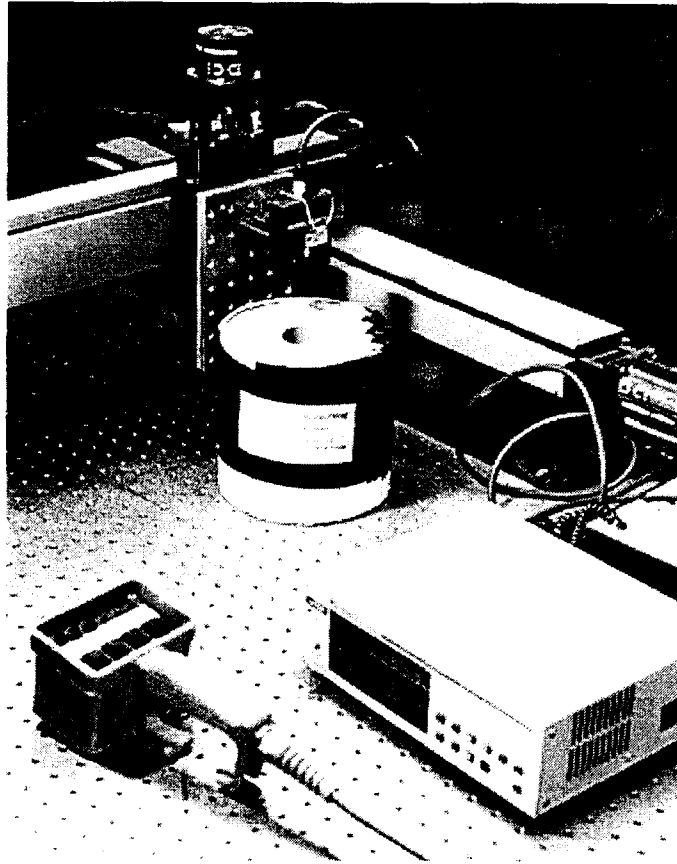


Figure 6. Photograph of material characterization experiment: inert propellant grain in fixture.

Self-correlation analysis was also performed to determine the length scale of surface displacement variations. These were found to be on order of the scan size, indicating that the surface is very uniform. A graph of the correlation analysis is presented in Figure 7.

Gray Modeling Clay. We used a blend of two colors of Sculpey™ II to create a test sample that closely matched the color and reflectance of the simulated propellant. After kneading this sample to insure uniformity, we pressed it against a flat plate to create a smooth surface. This sample was then placed in the test fixture at the same vertical displacement from the sensor as the simulated propellant. Three linear scans were then performed. The mean value of the scaled reflected radiance was found to be 0.070. A self-correlation analysis was performed, and the variation in surface displacement was found to be on order of the length of the scan. These data are presented in Figures 8 and 9.

These data support the conclusion that Sculpey™ II modeling clay is an excellent analog for building test specimens. We used this compound in all subsequent testing.

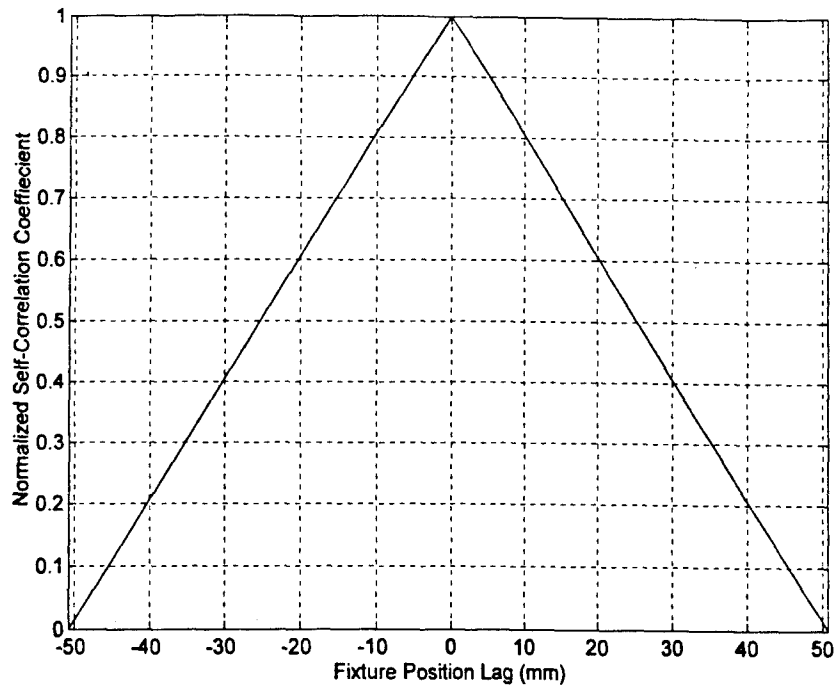


Figure 7. Self-correlation analysis of surface profile data from the inert propellant grain sample.

#### 4.1.2 Building Test Specimens

We experimented with several different methods for shaping the samples. As a first attempt, a spatula crafted in the shape of one of the SRM grain fins was made from 1.6-mm aluminum sheet. The spatula was then mounted on the robot and dragged through a block of clay, carving out a fin of the desired shape. However, this method produced excessive surface roughness in the samples and did not cut consistently for more than 10 mm in length. Since we desired samples up to 50 mm long, this method was deemed inadequate.

For a second attempt, we used the services of a sculpting consultant. After viewing our work, he proceeded to fabricate an assembly for creating the rocket fins by using specially shaped cutting tools, which presented a smaller cross-section than our spatula. The tool was incrementally lowered into the clay after each cutting pass. This method allowed us to make up to a 200-mm length of simulated SRM grain with a very smooth surface.

Large and Small Models. The two different sizes of samples were created in order to test the capabilities of two optical triangulation engines. Templates for the cutting tools used to make these samples are shown in Figures 10 and 11. The small-model sample (Figure 10) has a depth of approximately 15 mm, which matches the range of the Keyence sensor. The large-model sample (Figure 11) is approximately 35 mm deep to match the range of a laser-based sensor built by QUEST. Both models were made in essentially the same shape as derived from parameters provided by our sponsor.

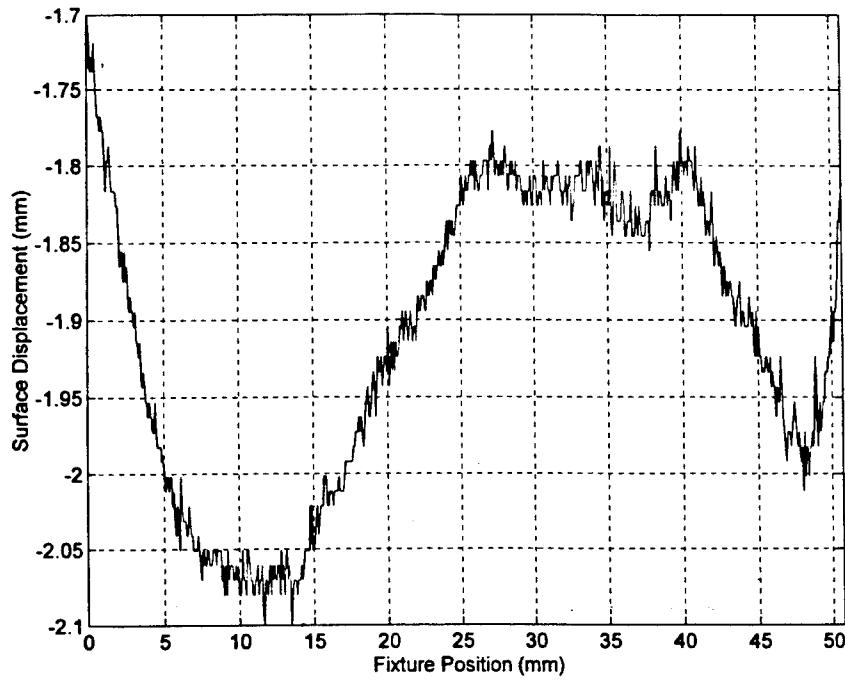


Figure 8. Surface profile of Sculptey™ II modeling clay.

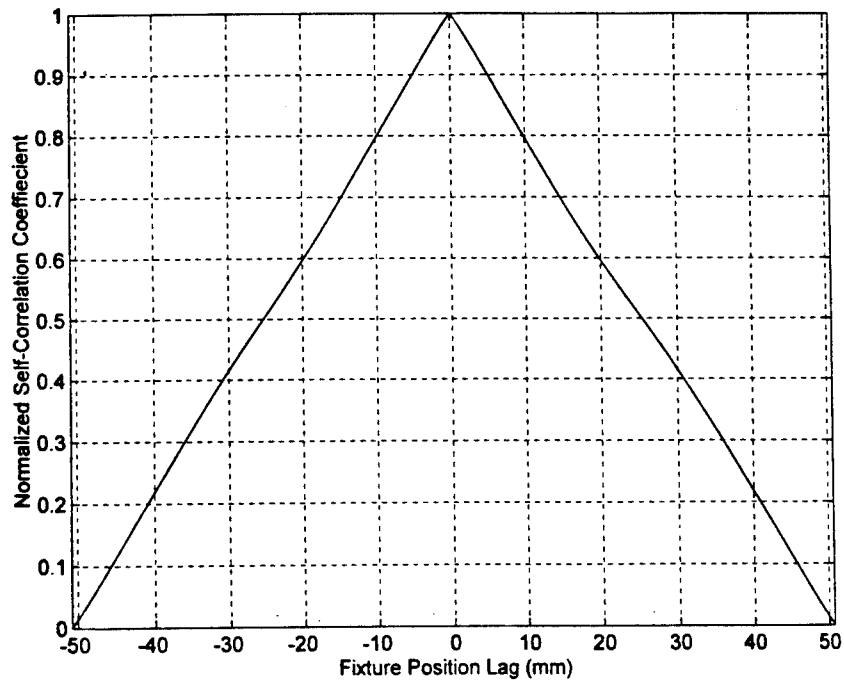


Figure 9. Self-correlation analysis of surface profile data from the Sculptey™ II modeling clay sample.



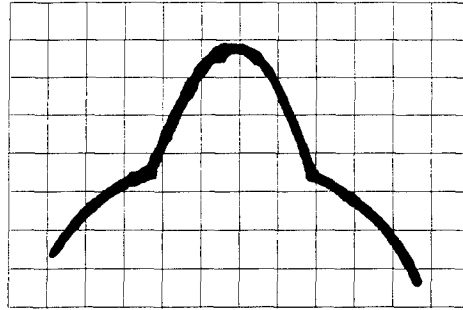


Figure 10. Template for small-model cutting tool.

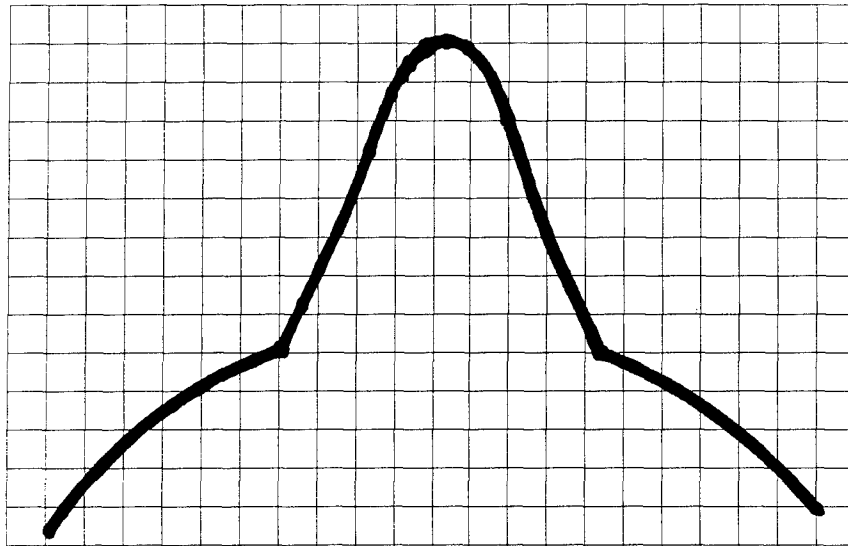


Figure 11. Template for large-model cutting tool.

Simulation of Cracking and Slumping. Cracking and slumping were simulated by several different methods. Pure slumping can be demonstrated by twisting a sample before curing, causing it to exhibit a smooth torsional deviation. Samples which were twisted after curing generally exhibited cracking in the surface as well as some slump. Pure cracking was simulated by inserting a thin-bladed knife into the sample after baking and then twisting. This causes a long, narrow crack with little normal displacement between the two sides. Cracking was also simulated by hard curing the samples and then shattering them with a hammer. Usually, this resulted in the loss of at least half of the sample length, but caused very fine cracking.

Simulation of Propellant Migration. Attempts were also made to simulate nitroglycerin leeching by placing water droplets on the surface of the samples prior to scanning with the OTE. However, it was found that the water was absorbed into clay during the course of a scan. We settled then on using droplets of 5-minute epoxy. The size of the epoxy droplets can be easily

varied from approximately 2 to 6 mm in diameter. The locations of the defects are also easily quantified, allowing us to match test data to the actual defects. It was our intention to locate propellant migration by sensing deviations in reflected intensity from the sample; however, the reflective properties of 5-minute epoxy are not known to us.

## 4.2 METHOD OF EVALUATION

### 4.2.1 Laboratory Setup

A diagram of the experimental setup is shown in Figure 12, and a photograph is included as Figure 13. The laboratory setup consisted of a 486 PC running QUEST's proprietary FIXTURE.EXE software. This software controls both the four-axis robot and a Keithley-MetraByte DAS-8 data acquisition board. This board has eight analog inputs, which offer 12 bits of sensitivity over a range of  $\pm 5$  volts. The robot has three Cartesian axes and one rotational axis. The three Cartesian axes have resolution and repeatability to 0.0025-mm; the rotational axis to 0.09 degrees. Data were taken by using a raster scan and  $z$  and  $\omega$  (refer to Figure 12 for coordinate axes). The sensor was attached to the rotational stage of the robot, enabling us to mimic the functionality of the proposed inspection system. Scans were taken over a single fin of simulated SRM propellant. Using the post-processing routines described below in Section 4.2.2 we were able to reflect this data around its axis of symmetry in order to obtain a simulated, full bore scan.

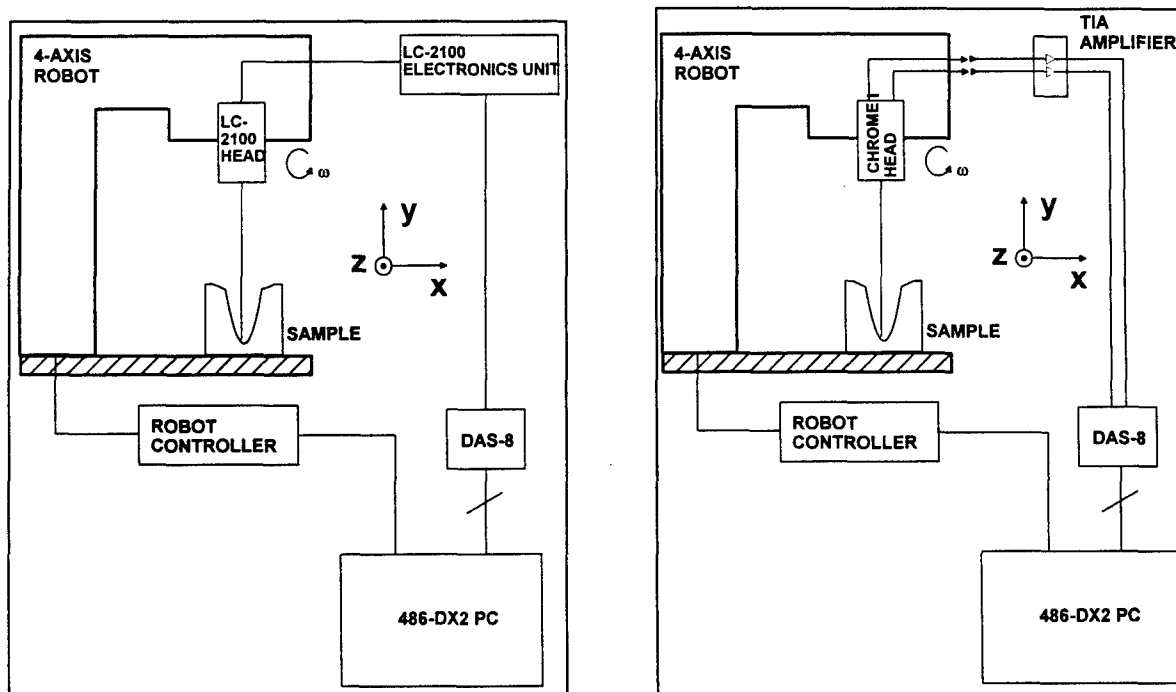


Figure 12. Diagram of experimental setup.

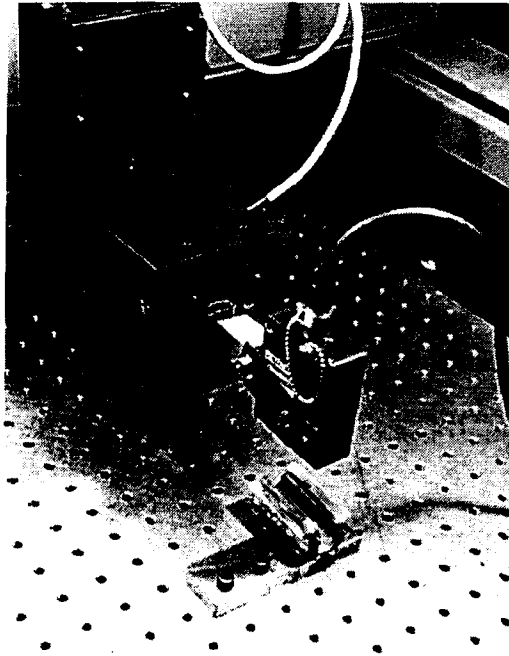


Figure 13. Photograph of experimental setup.

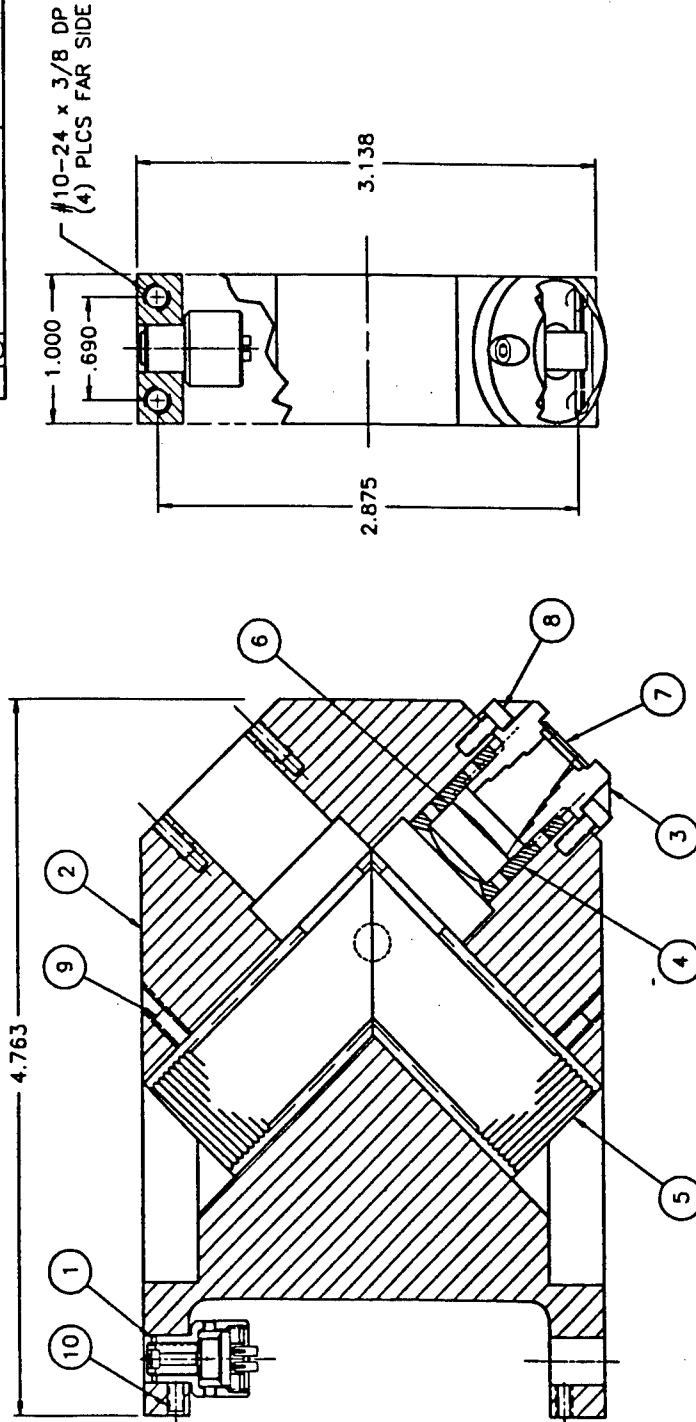
Two different optical triangulation sensors were tested: a Keyence Corporation LC-2100 and a QUEST-built sensor. These sensors have different range and resolution capabilities. Thus, two different-size models were fabricated in order to properly test each instrument.

Commercial Optical Triangulation Sensor. The Keyence LC-2100 is a commercially available optical triangulation sensor with resolution sensitivity of 0.5 micron and a range of 16 mm centered on a 50-mm standoff. It has automatic, variable gain control, enabling it to measure displacement from objects with a wide range of surface reflectivity. The LC-2100 is capable of measuring both the total reflected signal and displacement, although not simultaneously. It has a single analog output on the rear panel, which generates a signal linearly proportional to the desired measurement. Reflected return is expressed as a fraction between 0 and 1. For our tests, the analog output of the LC-2100 was run into the DAS-8 data collection board on the host PC.

QUEST Optical Triangulation Sensor. A second sensor used for testing the propellant samples was designed and built by QUEST. The following discussion will assume familiarity with the theory of operation of optical triangulation sensors (refer to Section 2.3).

An assembly drawing of the probe head is shown in Figure 14. The sensor has a measurement range of 36 mm centered around a standoff of 40 mm. The laser (Item #1 in Figure 14) is driven by a precision current source. The signals from the lateral-effect photodiode are fed through a variable gain transimpedance amplifier and into two channels on the DAS-8 board. The gain is adjusted manually in order to yield valid signals for the measurement surface.

PARTS LIST			
QTY	ITEM	DESCRIPTION	SPECIFICATION
1	(1)	PROBE LIGHT SOURCE SUB-ASSEMBLY	
1	(2)	TEST BODY	65472
1	(3)	DETECTOR HOLDER	65473
1	(4)	LENS HOLDER	65474
2	(5)	LIGHT SHIELD	65475
1	(6)	LENS	
1	(7)	LATERAL CELL	60808
2	(8)	SWISS FA-40 = 1/4	AS ANVL
2	(9)	SWISS FB-32 = 1/4	AS ANVL
1	(10)	SWISS FA-40 = 3/16 OR LONGER	AS ANVL



CENTERLINE SECTION

TOLERANCES  
DIMENSIONS ARE FOR  
REFERENCE ONLY

Figure 14. Assembly drawing of in-house optical triangulation head.

Since this probe is not a self-contained unit like the LC-2100, it must be calibrated. A calibration curve is the set of points representing the value of the parameter  $x$  from Equation (5) versus the known distance to the measurement surface  $y$ . This curve is obtained by mounting the probe on the robot, stepping the robot away from a measurement surface at known intervals  $\Delta y$ , and recording the signal levels  $I_1$  and  $I_2$ . Using a mathematical analysis package, such as MATLAB, a polynomial  $y = P(x)$  is fit to the data, which captures the shape of the calibration curve. Henceforth, for a given value of  $x$ , a measured displacement  $y$  may be calculated. Figure 15 shows the calibration curve for the in-house probe. Observing the standard deviation of the probe at a fixed position relative to the measurement surface, we calculated that the probe has a one sigma resolution of 0.13 mm.

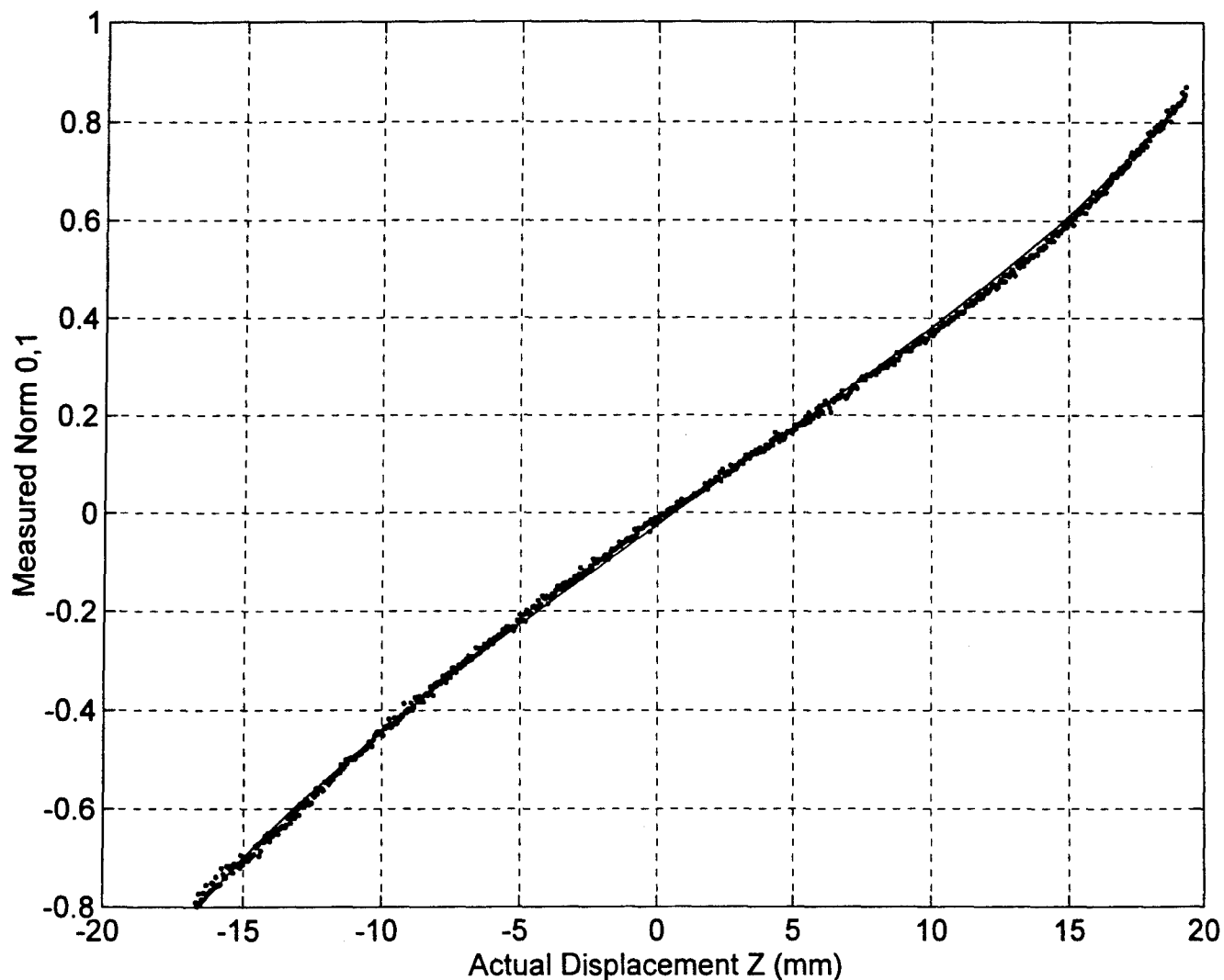


Figure 15. Calibration curve of the in-house probe (solid line represents the calibration polynomial).

#### 4.2.2 Analysis Facilities

To analyze the data and present it in a form similar to the proposed inspection system, a series of scripts were developed to locate defects and generate graphical displays. These scripts are listed in the Appendix. The images presented below were processed using MATLAB for Windows 4.2b. Using a 386-33 PC compatible on a 3000-point original set, the processing time is approximately one minute. The algorithms for performing this operation are arrayed as a pipeline, that is, data are fed through successive transformations.

All transformations  $(X, Y, Z) \rightarrow (R, \theta, Z)$  are performed using the standard  $3 \times 3$  transformation matrix

$$\begin{pmatrix} \cos \alpha & \sin \alpha & 0 \\ -\sin \alpha & \cos \alpha & 0 \\ 0 & 0 & 1 \end{pmatrix} \quad (6)$$

- HEAD2NAT.M: Head2nat transforms raw data  $(r, \omega, z)$  from scans using QUEST's FIXTURE.EXE robot control and data acquisition software into the "natural frame" of reference. The natural frame is a Cartesian coordinate system with the origin placed at the emission point of the beam. All measurements are in millimeters. Head2nat requires as input the data stream, standoff distance, and conversion factor for raw units to millimeters. For the Keyence sensor, the standoff is 50 mm, and the conversion factor is 2. Three matrixes,  $X$ ,  $Y$ , and  $Z$ , are returned with an  $(x, y, z)$  ordered pair for each offset  $(i, j)$ . The  $i$  index runs from 1 to the number of points in  $\omega$ , and the  $j$  index runs from 1 to the number of points in  $x$ .
- DETOFF.M: Detoff determines the offset in  $x$  that is required for the scan from the robot to subtend an angle  $360/n$ . It uses the mean of all points in  $z$  along the edge of the groove to determine the angle. The angle is defined as

$$\text{atan}(y_1/x_1) + \text{atan}(-y_2/x_2) \quad (7)$$

for  $(x_1, y_1)$  the average last point on the left edge and  $(x_2, y_2)$  the average last point on the right edge. The return value, *off*, is the offset in  $x$  such that the transformation

$$X' = X - \text{off} \quad (8)$$

yields a data matrix that subtends the angle  $360/n$ . Since *atan* is a transcendental function, *detoff* closes in on an ideal value of *off* using a binary search method, which insures rapid convergence.

- NAT2RT.M: Nat2rt transforms the Cartesian data matrixes  $X$  and  $Y$  to the cylindrical data matrixes  $R$  and  $\Theta$ . It accepts an offset (the return value from detoff) that is subtracted from the  $X$  matrix.
- RTMIRROR.M: This routine reflects the scan through its axis of symmetry to create simulated full-section bore scans. First, the scan is offset in  $\theta$  such that it lies between 0 and  $360/n$ . Then it is reflected about the axis  $\theta = 360/n$ . Note that after this transformation, the data matrixes have the same value of  $r$  at  $\theta = 0$  and  $180/n$ , insuring continuity along the scan. This slice is successively rotated about the  $\theta_{max}$  axis until  $n-1$  reflections are performed. For  $i \times j$  input matrixes  $(R, \Theta)$ , the transformed matrix is dimension  $(n \cdot i - 1)j$ .
- RT2NAT.M: Rt2nat is the inverse of nat2rt and transforms the cylindrical data matrixes  $[R(Z), \Theta(Z)]$  to Cartesian data matrixes  $(X, Y, Z)$ .
- PLOTNAT.M: Plotnat plots any set of natural coordinate data matrixes  $(X, Y, Z)$  as a meshgrid.

Data Pipeline. A pipeline M-file, TRANS.M runs through these transformations successively in order to ease processing. It accepts as input the raw data stream from FIXTURE.EXE, the standoff distance, the conversion factor, and  $n$ , and it returns the natural coordinates of the scan and the natural coordinates of the simulated full bore scan.

Flaw Detection. Automated flaw detection was performed in a simplified manner for this demonstration. There were two primary methods used, both based upon the difference of a moving average from the data. Fourier analysis, a likely candidate for flaw detection in the final system, was not examined. All flaw detection routines are based upon the raw data from the sensor in robot coordinates  $R(\omega, z)$ .

The surface deviation method is excellent for detecting discontinuities in the surface such as cracking and propellant migration. In this method, a fifteen-point unweighted moving average is run over the data in the  $z$  direction. By running in  $z$ , we obtain points of approximately equal displacement  $r$ , ensuring continuity. The moving average is then subtracted from the original data set to show deviations between the actual and “expected” surface. For display, the squared deviation at each point may be color mapped and superimposed on the meshgrid surface representing the data set. This method was found to be the most keenly sensitive to surface deviations caused by cracking and localized slumping. However, spikes in the data at crack points cause the moving average to “trail” across these features. For this reason, the reader may notice some smearing of the color mapping around flaws in the plots that use the surface displacement method (see Figure 16).

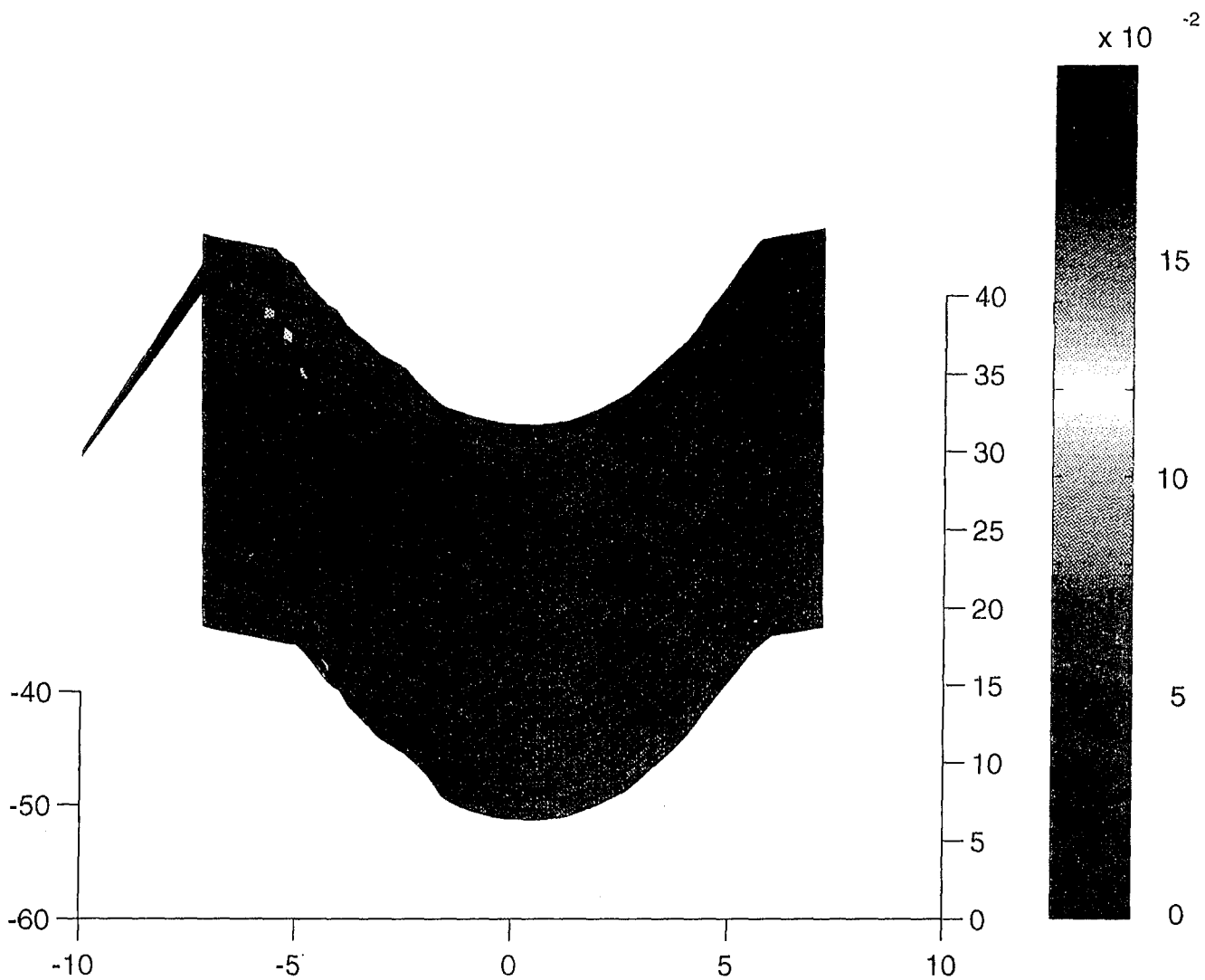


Figure 16. Full fin scan of Sample #2.



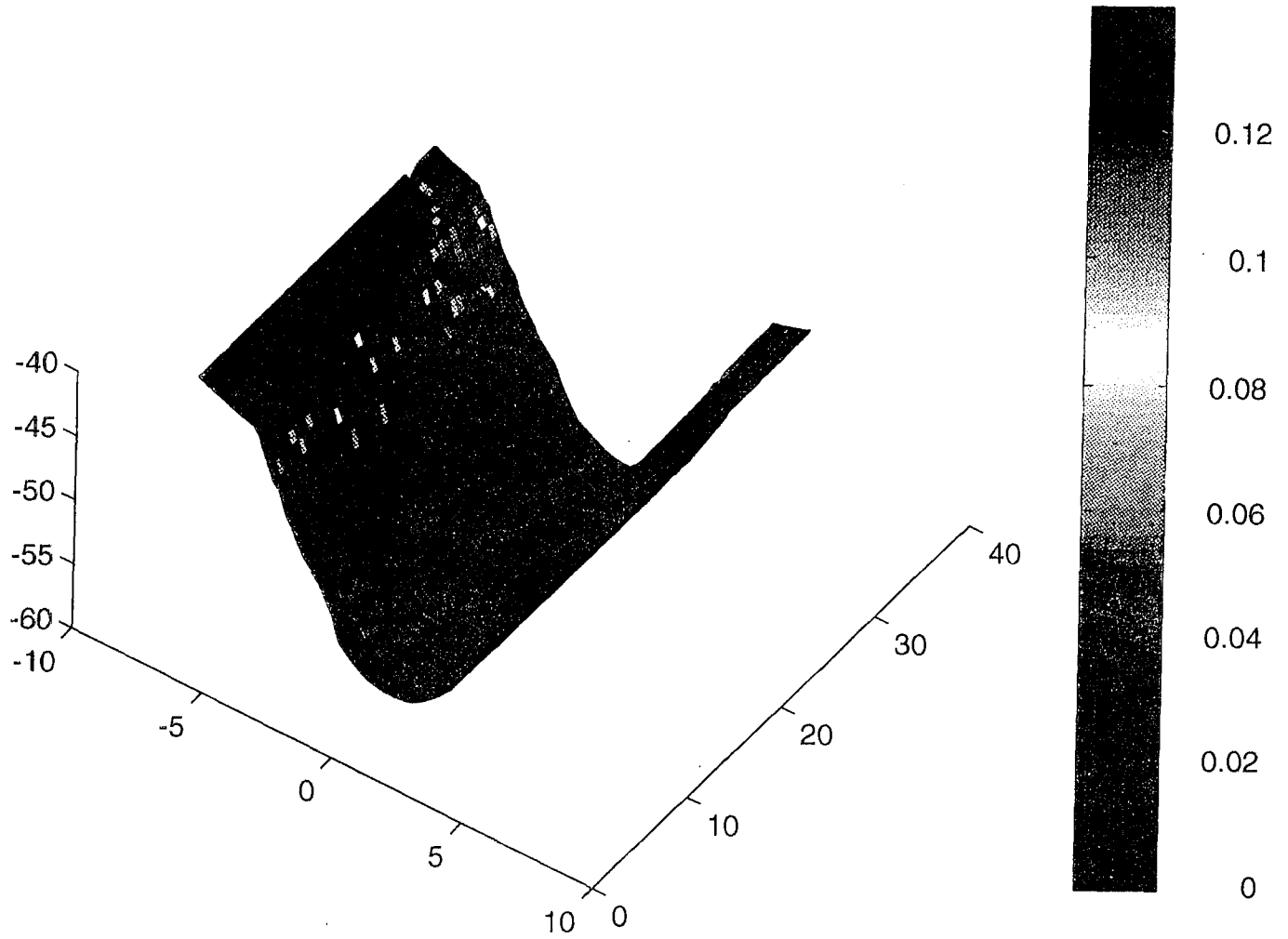


Figure 16. Full fin scan of Sample #2 (Cont.).

The reflected radiance deviation method showed acumen for detecting cracks. In future systems, it may also be used to locate propellant migration, although the current study did not provide evidence that this would be effective. When the beam is incident directly upon a spot with greatly different reflectivity than its surroundings, such as a crack or droplet, it causes a change in the total radiance levels ( $I_1 + I_2$ , called "sum levels") of the detector. These data are processed by the same method of differencing described above. Reflected radiance data may be recorded in one scan with the in-house OTE, but two passes with the Keyence OTE are required.

Automated detection of slumping was not addressed due to the nature of the problem. Slumping is characterized by large-scale deviations of the surface from the expected value. Such deviations are not observable with the short-range moving average method described previously. In a test fixture, large-scale deviations would be possible to detect with a properly aligned, point-to-point matched reference surface. As another method, a full bore scan could employ Fourier analysis to detect aperiodicity due to large-scale deviations. By adjusting the viewing angle of the plotted data, slumping is easily visible to the reader (see Figure 16).

### 4.3 TEST RESULTS

#### 4.3.1 Small Model

The small-model template is shown in Figure 10. Figure 17 shows the resulting scan of a flawless small-model sample (#1) using the Keyence sensor. The color data shows the deviation of the actual surface from expected values using the surface deviation method described previously. A photograph of this sample is also included in Figure 18. As can be seen, some surface roughness is caused by the abrading of the cutting tool against the fin side wall. This roughness causes the strip of color along the side wall visible in Figure 16. We felt that smoothing the part manually would result in a greater perturbation than leaving it alone.

Figure 19 shows a simulated full bore scan of Figure 17. Color is neglected for clarity. This is one of the views that the proposed Phase II system would be capable of displaying.

Cracking and Slumping. Figure 16 depicts a full fin scan of Sample #2, with color representing surface deviation. This sample was twisted after baking and has a long thin crack on one of the fin faces, in addition to some slump caused by the torque. The spike on the left side of Figure 16 is caused by a missing data point. This is at the deepest part of the crack; the beam is totally absorbed at this location. Photographs of this crack are shown in Figure 20. It can be seen that the surface deviation method is able to discriminate the crack. This particular crack is in the most difficult location for an optical triangulation sensor to detect. At this angle, the beam is

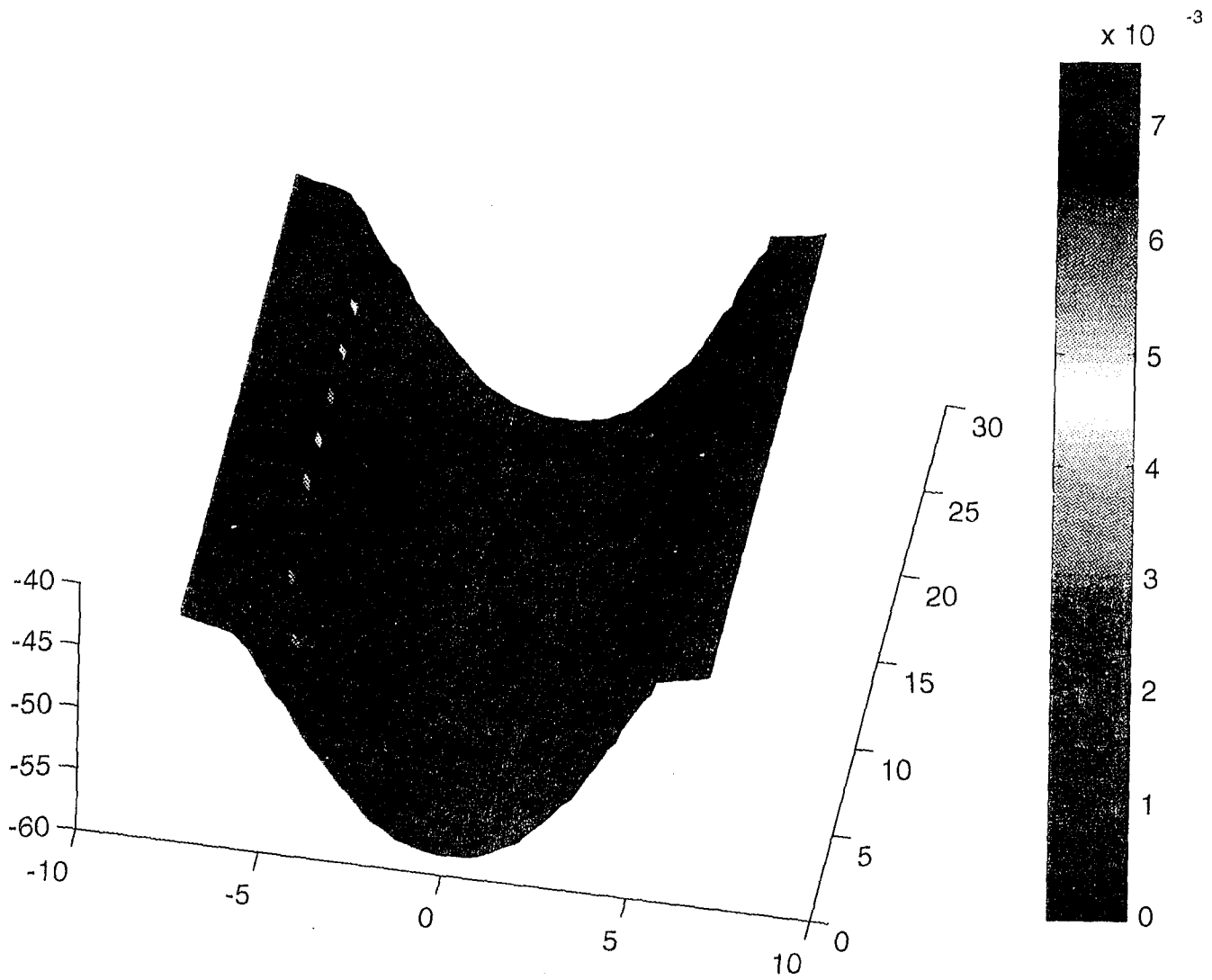


Figure 17. Full fin scan of Sample #1.

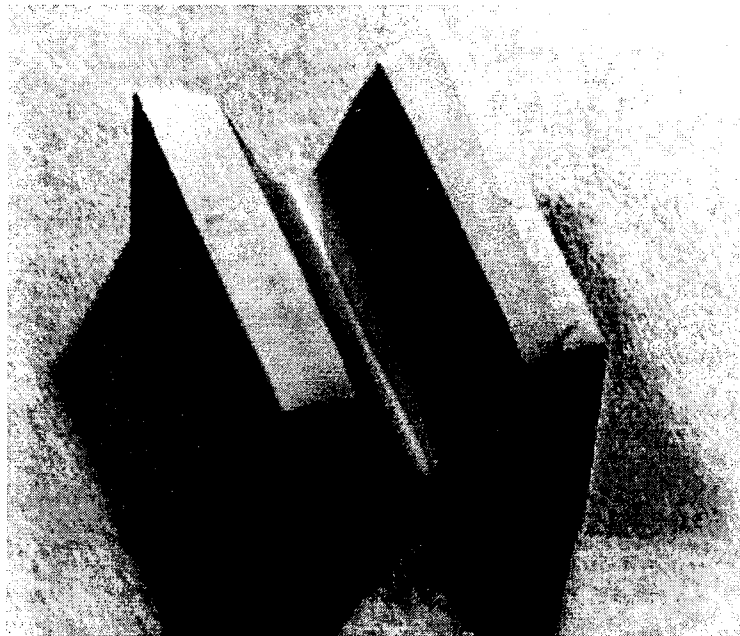


Figure 18. Photograph of Sample #1.

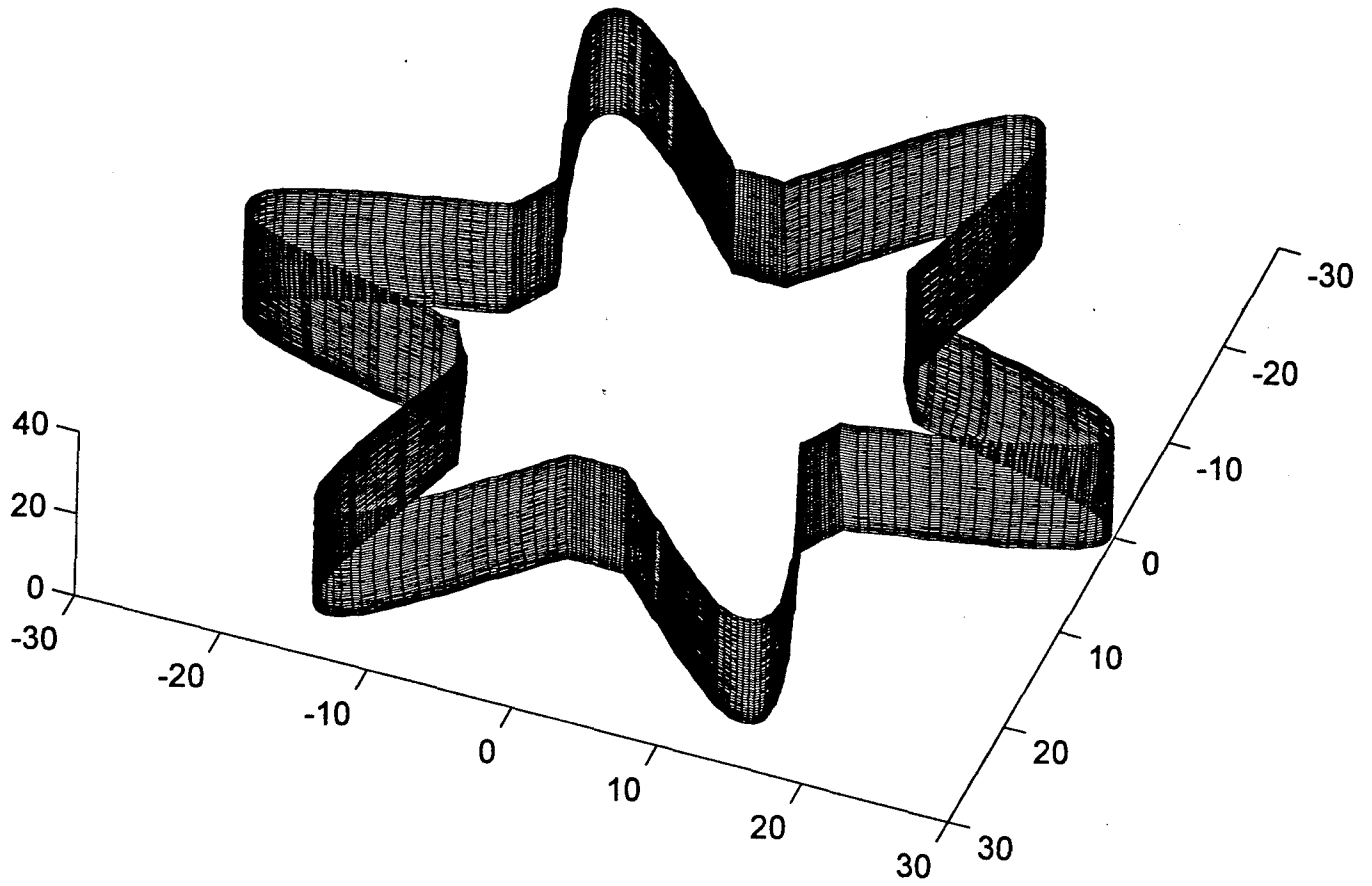


Figure 19. Simulated full bore scan of Sample #1.

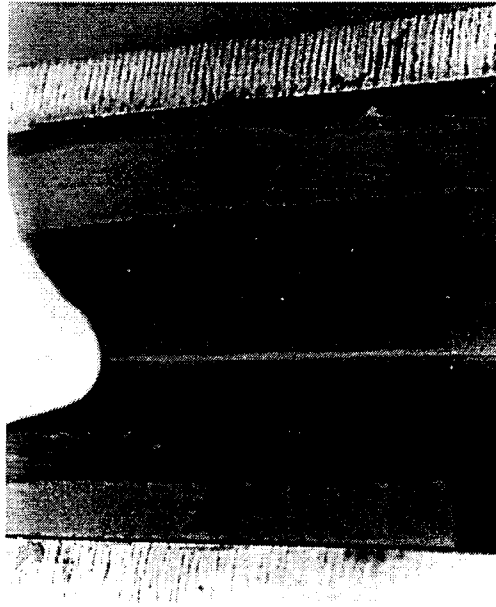


Figure 20. Photographs of crack in Sample #2.

incident about  $40^\circ$  from the tangent to the surface. The ability of this sensor to locate this feature is a positive development for the Phase II device.

A higher resolution scan of the crack in Sample #2 is shown in Figure 21. The scan resolution is  $0.09^\circ$  in  $\omega$  and 0.23 mm in  $z$ . Corrected for standoff, this would yield 1320 points in circumference. The axial density is approximately twice the LC-2100 spot size.

This sample also shows evidence of slumping. Reviewing Figure 21, the reader should notice a slight turn in the rim of the fin to the left of the crack all the way to the end of the sample. This is a result of twisting the sample as discussed above, and it is analogous to slumping in an SRM sample. In Figure 16, it can be seen that the lines of equal angle are not parallel to the  $z$  axis. This is the graphical manifestation of slump.

Another crack that was located and analyzed on the small-model setup was Sample #3. This sample was sandblasted after baking in order to simulate the effect of surface ammonium nitrate crystals. A photograph of this crack is shown in Figure 22, and the scan is shown in Figure 23. It can be seen that this crack is also detectable despite the increased point-to-point variability.

Propellant Migration. As discussed above, propellant migration was simulated by epoxy droplets hardened on the surface of the sample. We placed five droplets of various sizes at different elevations on Sample #2. A photograph of the sample is shown in Figure 24 for visual correlation.

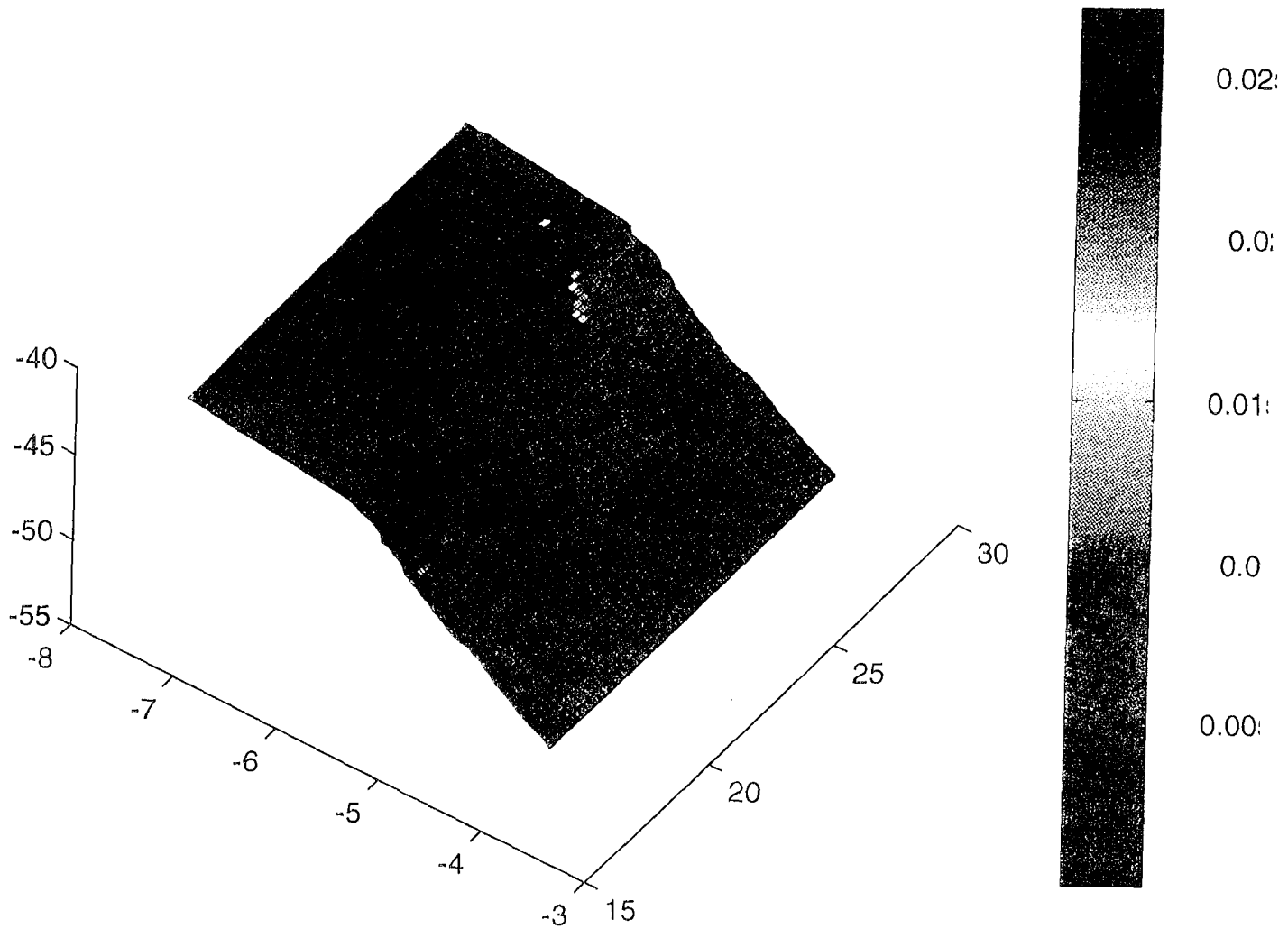


Figure 21. High-density scan of Sample #2 in neighborhood of crack.

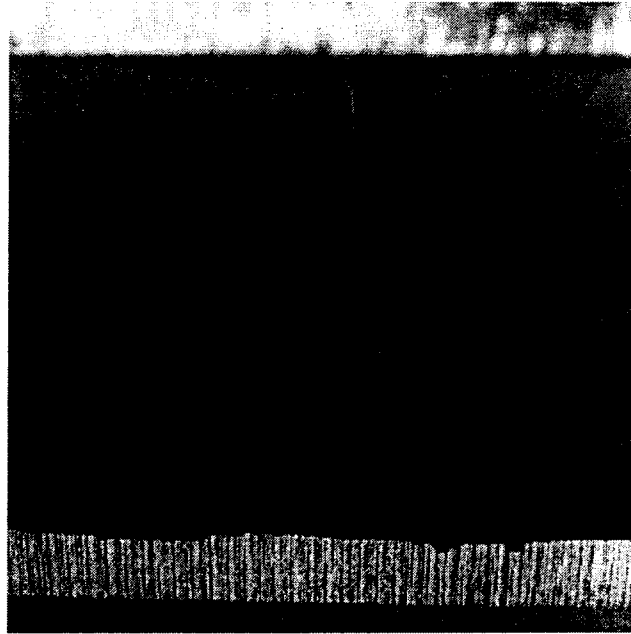


Figure 22. Photograph of crack in Sample #3.



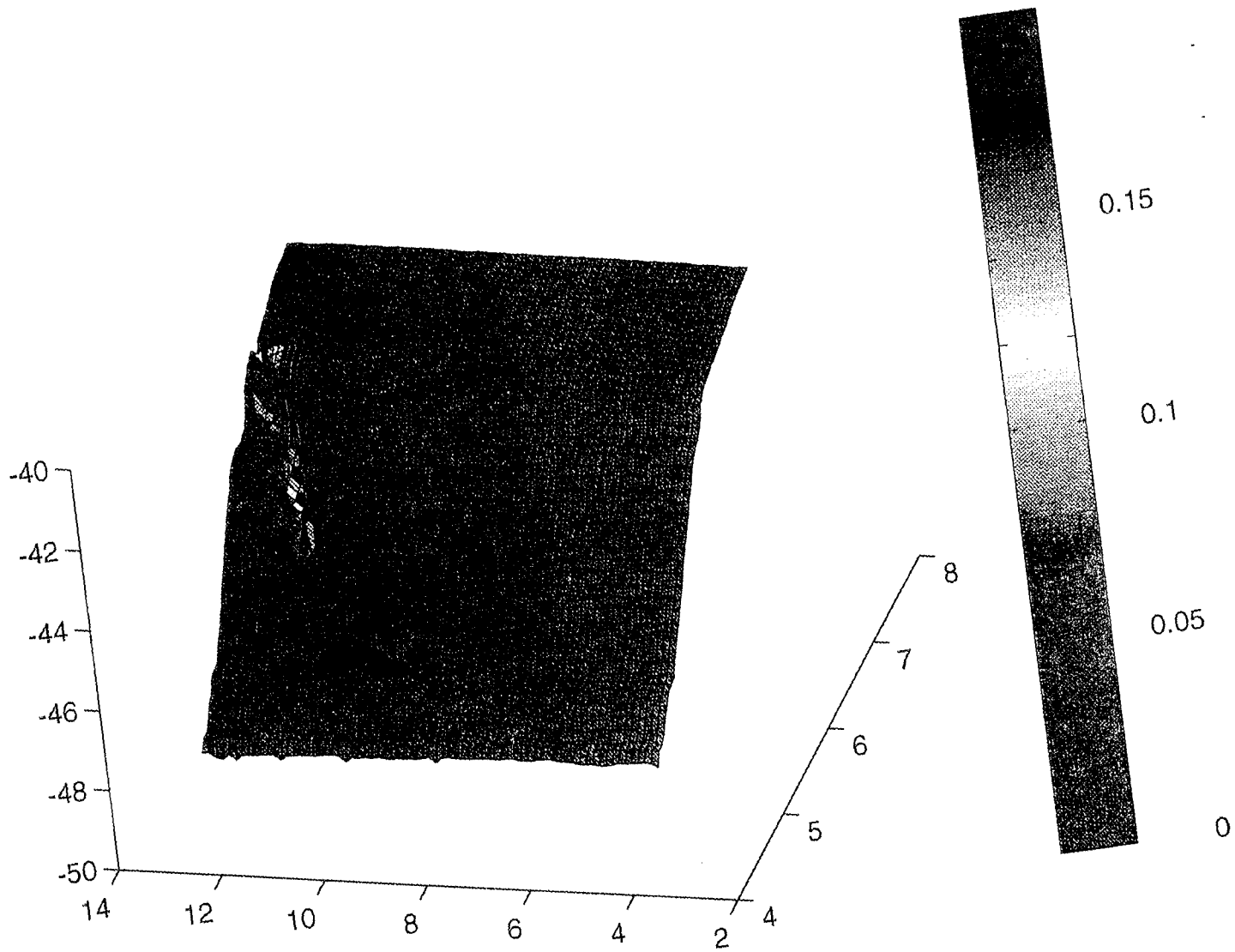


Figure 23. High-density scan of Sample #3 in neighborhood of crack.

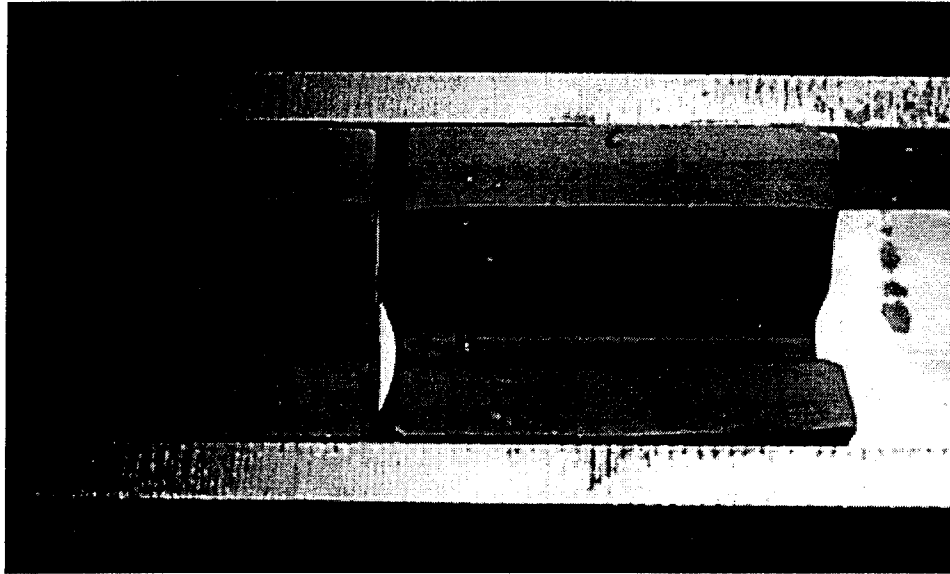


Figure 24. Photograph of Sample #2 with surface deviated flaw detection.

Two methods of automated flaw detection were applied to this data set: surface deviation and reflected intensity variation. Plots are presented in Figures 25 and 26. As can be seen, the surface deviation method appears to be a more robust flaw detection system.

#### 4.3.2 Large Model

The large-model template is shown in Figure 11. Figure 27 shows the resulting scan of a flawless large model using the QUEST-built sensor. Figure 28 is a simulated full-bore scan constructed from this data. The color data shows the deviation of the actual surface from expected values using the surface deviation method described previously. A photograph of this sample is also included in Figure 29. Like the small-model sample, some surface roughness is visible in Figure 27, and it is caused by the abrading of the cutting tool against the fin side wall. However, this probe does not have the same resolution capabilities of the Keyence sensor, and some of the point-to-point variation is caused by the higher (0.13-mm) noise floor.

Figure 30 shows a scan of a crack flaw on the large-model sample. The crack origin is a very wide gap, while the crack type is very fine. In comparison to the photograph of this crack presented in Figure 31, it is apparent that this probe is not nearly as sensitive to microcracking as the Keyence sensor. Again, the high noise floor and large range conspire to hide much fine structure exhibited by the sample.

Because of the high noise floor, we elected not to perform high-density scans on microdefects present in the sample.

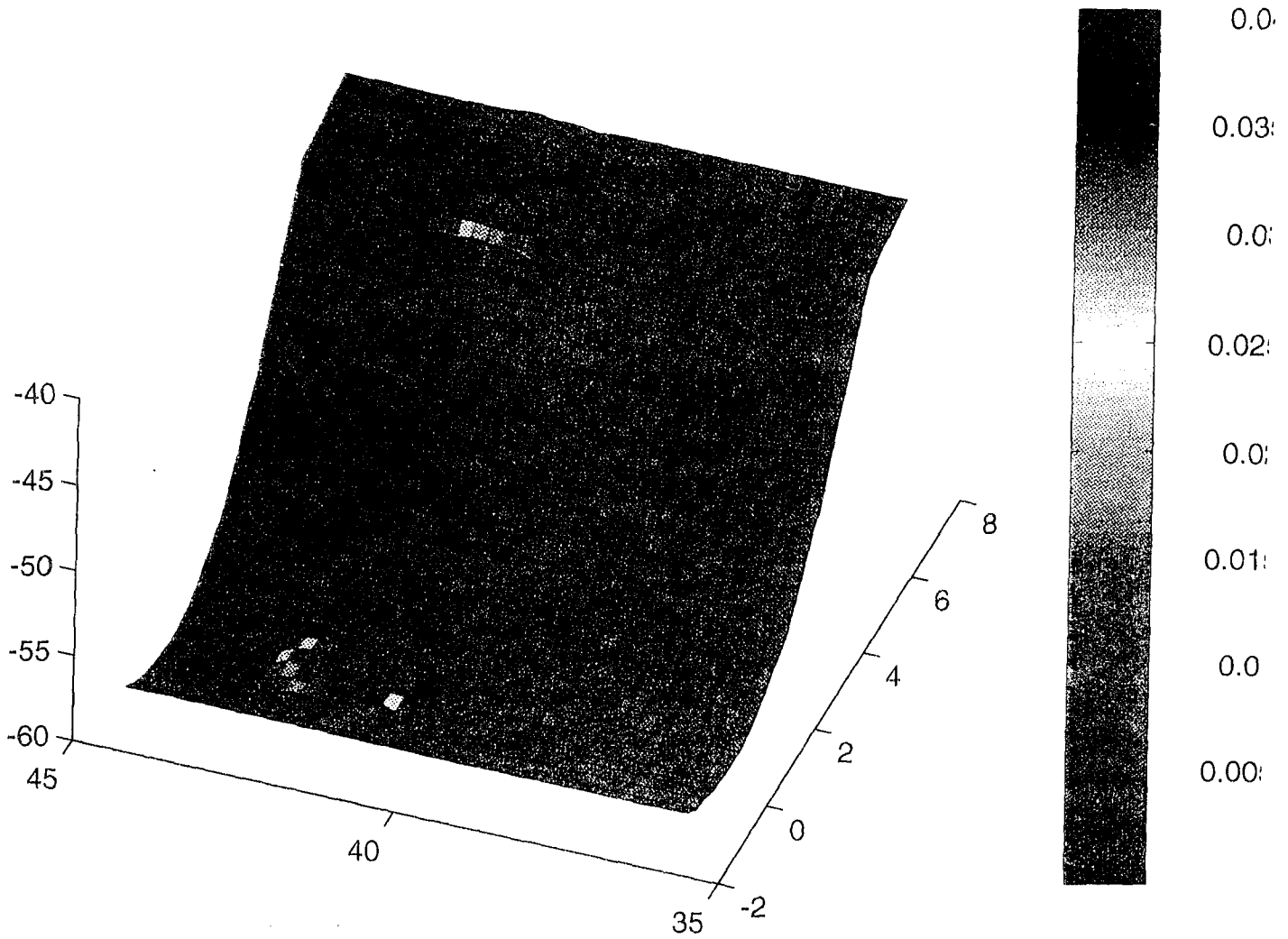


Figure 25. Scan of Sample #2 with surface deviation flaw detection.

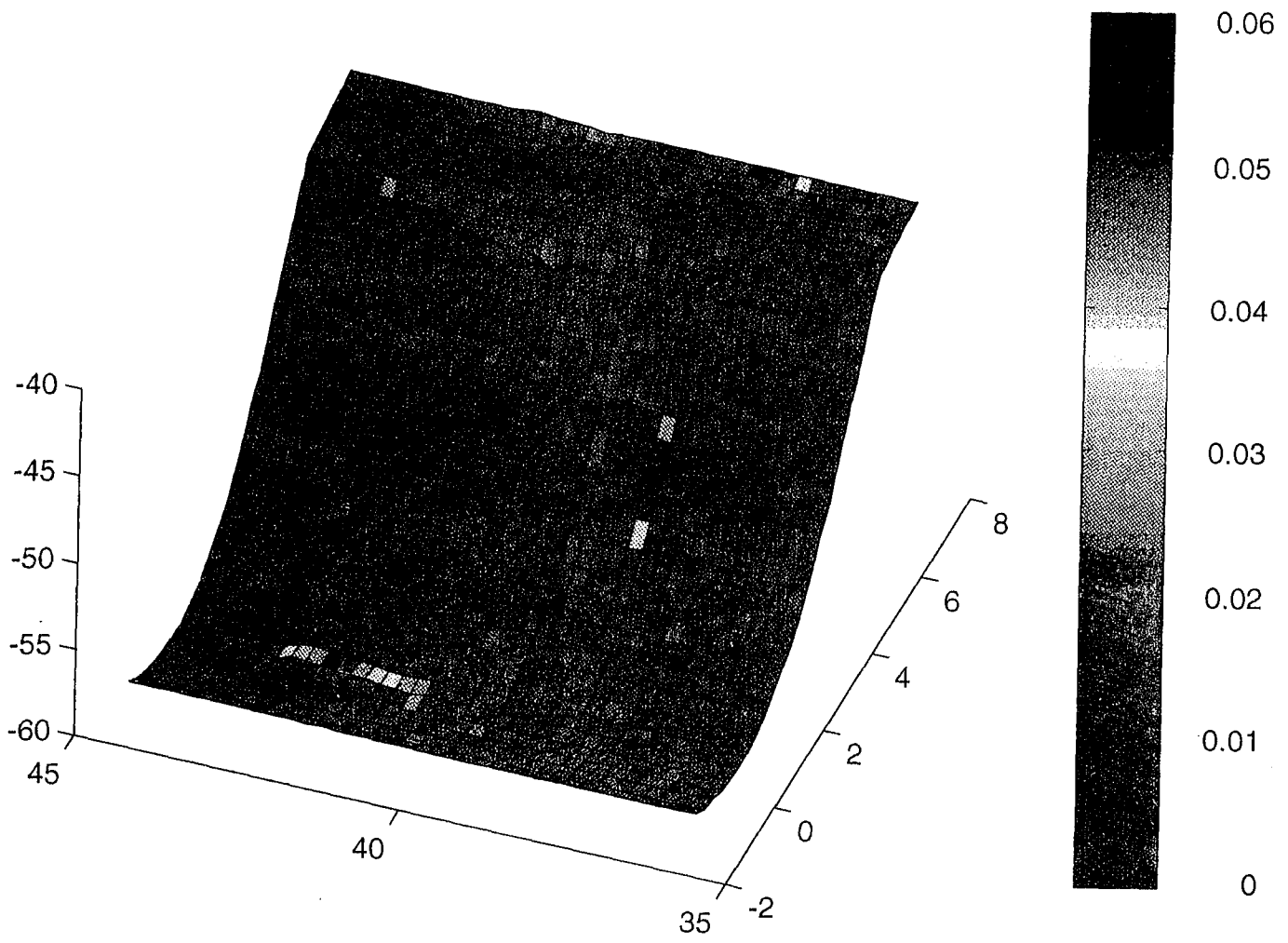


Figure 26. Scan of Sample #2 with reflected intensity deviation flaw detection.

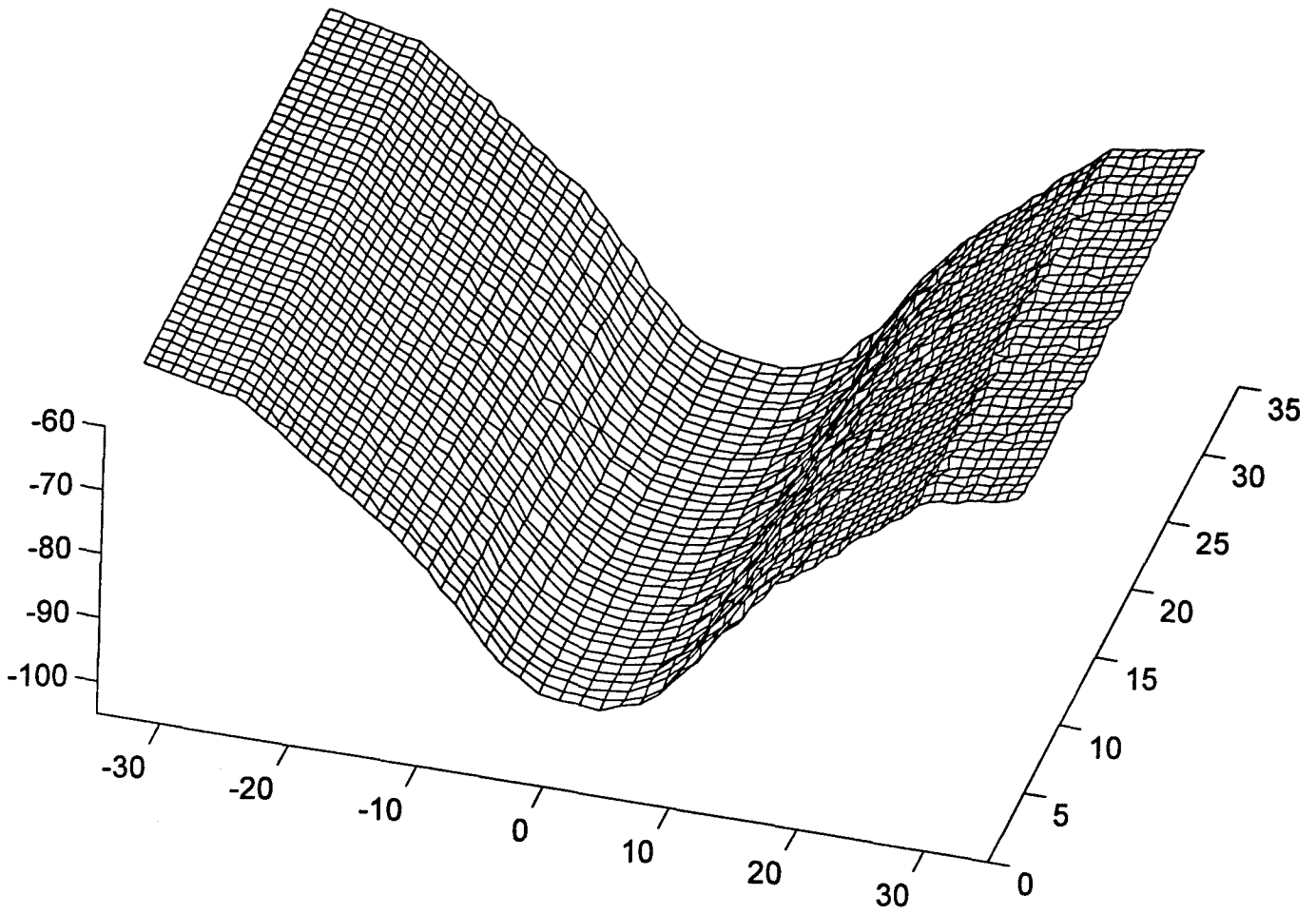


Figure 27. Scan of flawless large-model sample.

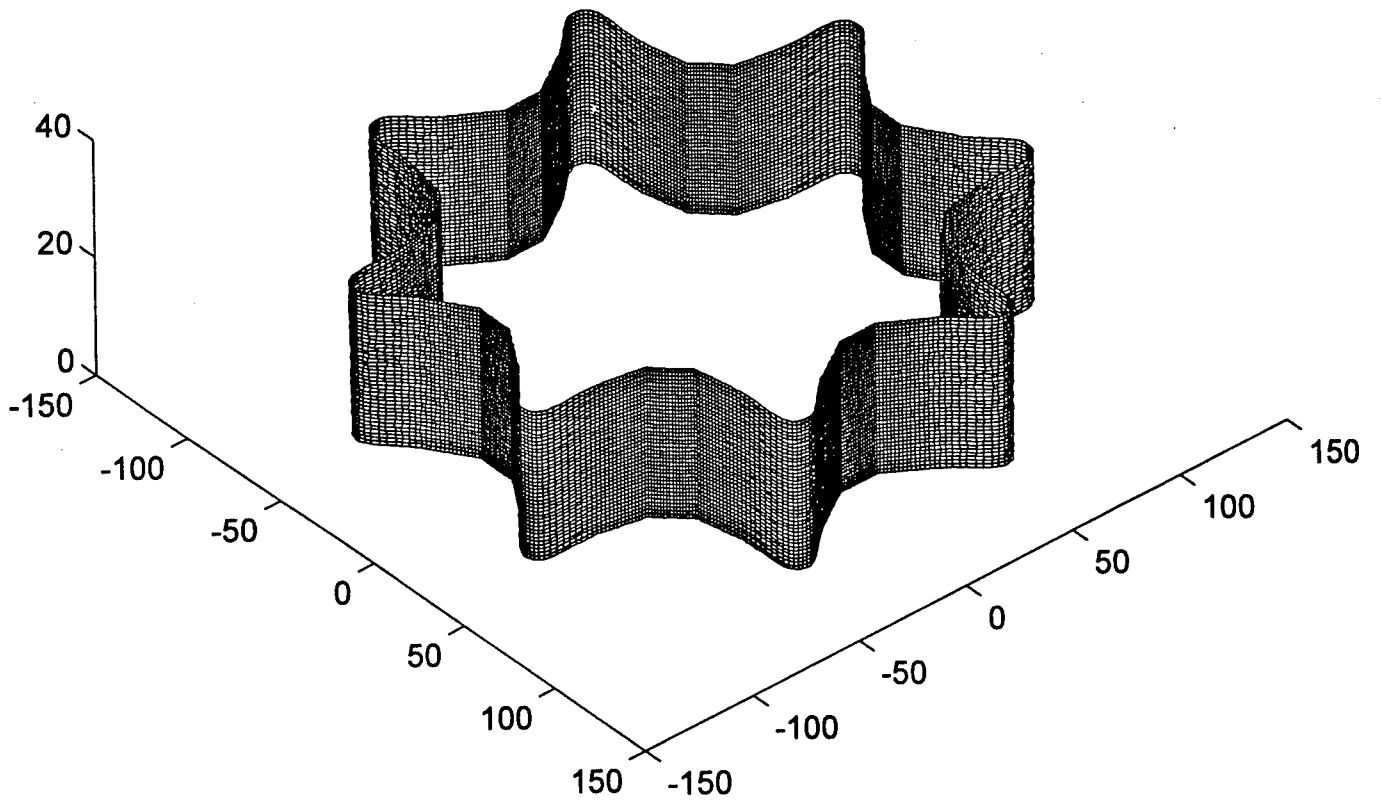


Figure 28. Simulated full-bore scan.

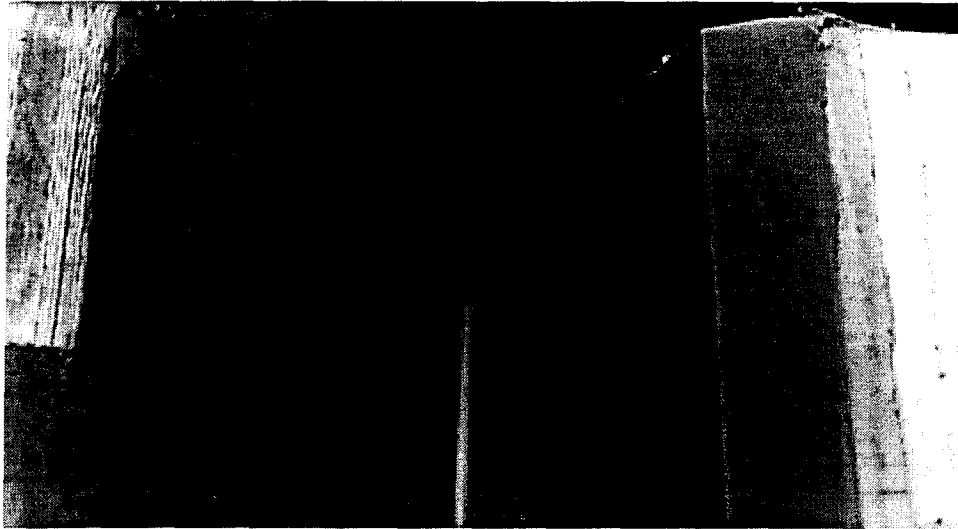


Figure 29. Photograph of large-model sample.

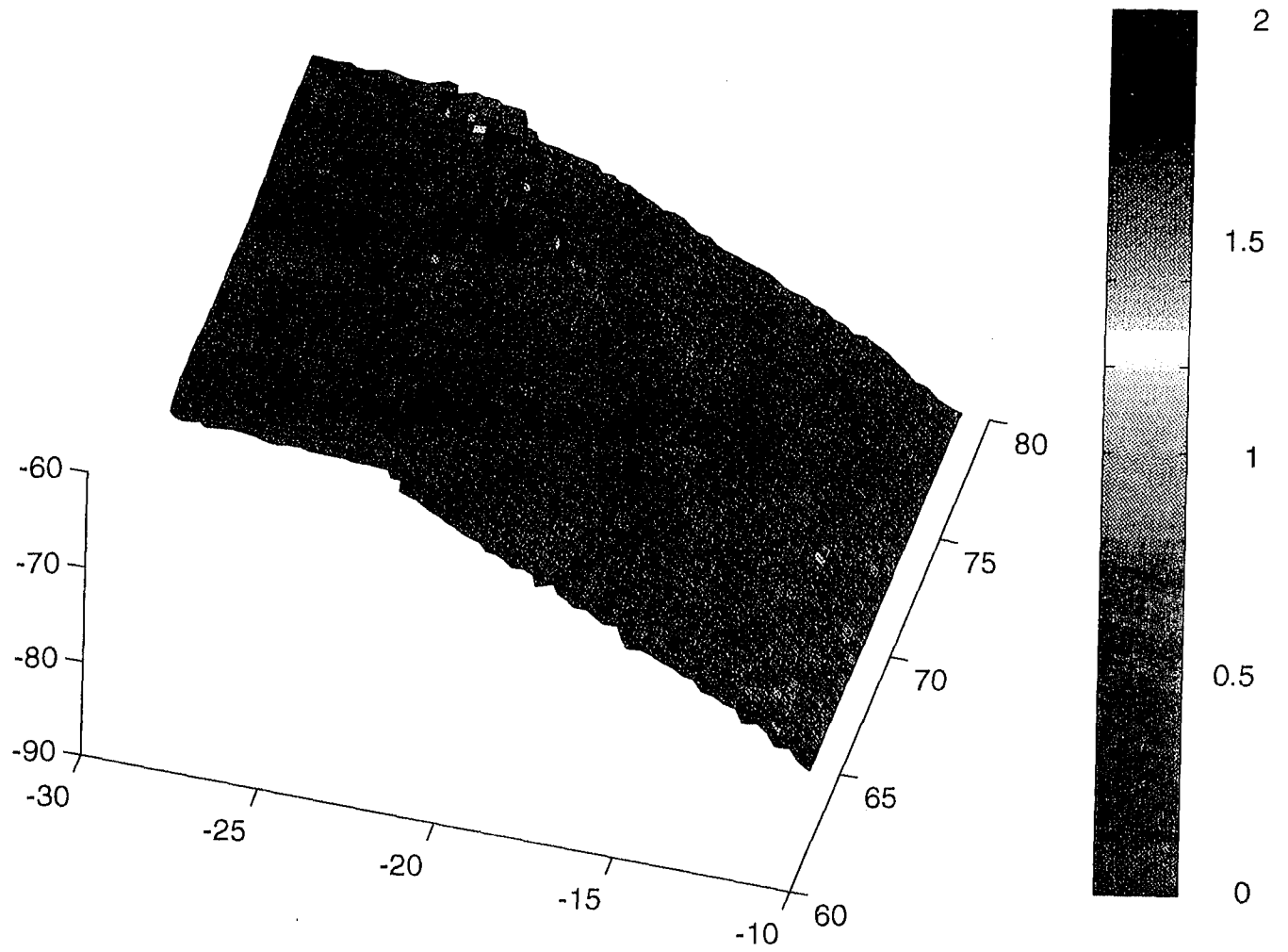


Figure 30. Scan of crack on large-model sample.



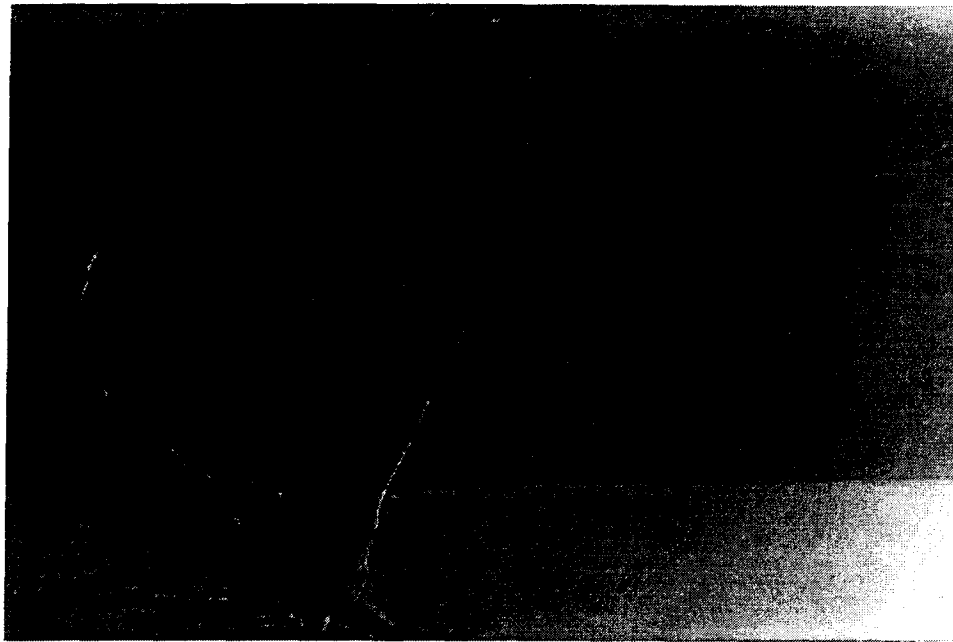


Figure 31. Photograph of crack present in large-model sample.

## 5. PHASE II PROGRAM DESCRIPTION

### 5.1 PHASE II TECHNICAL OBJECTIVES

The objective of the Phase II program will be to develop a lightweight, portable, and rugged system capable of conducting automated inspections of SRM's. The Solid Rocket Motor Inspection System (SRMIS) will be capable of rapidly obtaining accurate and quantitative data that will be used to generate a three-dimensional map of the motor. The fundamental system design will be based on field-proven systems that have been delivered to the U.S. Army, Navy, and Air Force.

Specific technical objectives of the Phase II program will include:

1. Developing a detailed system specification that will address functional, environmental, and safety requirements for the system.
2. Developing a system design that will meet the inspection needs of the U.S. Air Force and its civilian suppliers.
3. Demonstrating a prototype SRMIS in the laboratory and under field conditions.
4. Conducting a preliminary market study for a Phase III commercialization program.

### 5.2 PRELIMINARY DESIGN

The SRMIS will employ a rotating, laser-based sensor that will be automatically driven through the length of each test piece. The inspection system will include a laser-based sensor that will be capable of characterizing the internal surface of SRM's to a high degree of accuracy.

The sensor will be mounted on an extendible arm that will be supported outside of the motor housing. A hydraulic or pneumatic drive unit will provide both rotation and translation of the sensor assembly as it traverses along its inspection path, and high-resolution encoders will track the probe's angular and linear position for three-dimensional surface mapping.

All operations will be conducted using simple, menu-driven commands on a field-grade computer. Key functional components of the system will include:

- *Scanning Sensor Assembly* - A noncontact sensor that will rotate at 500 to 1000 rpm and translate through the length of the motor.

- *Delivery System* - A portable device to translate the sensors through the length of the rocket motor; this device will provide rotation, translation, and position encoding.
- *Data Display and Control Computer* - A field-grade industrial computer that will house the motor control electronics as well as the signal processing boards. The computer will then postprocess the inspection data and store it for analysis and archival.

The resulting automatic inspection system will significantly improve the U.S. Air Force's ability to monitor the condition of SRM's and ensure their safe storage and operation. A conceptual system diagram is shown in Figure 32.

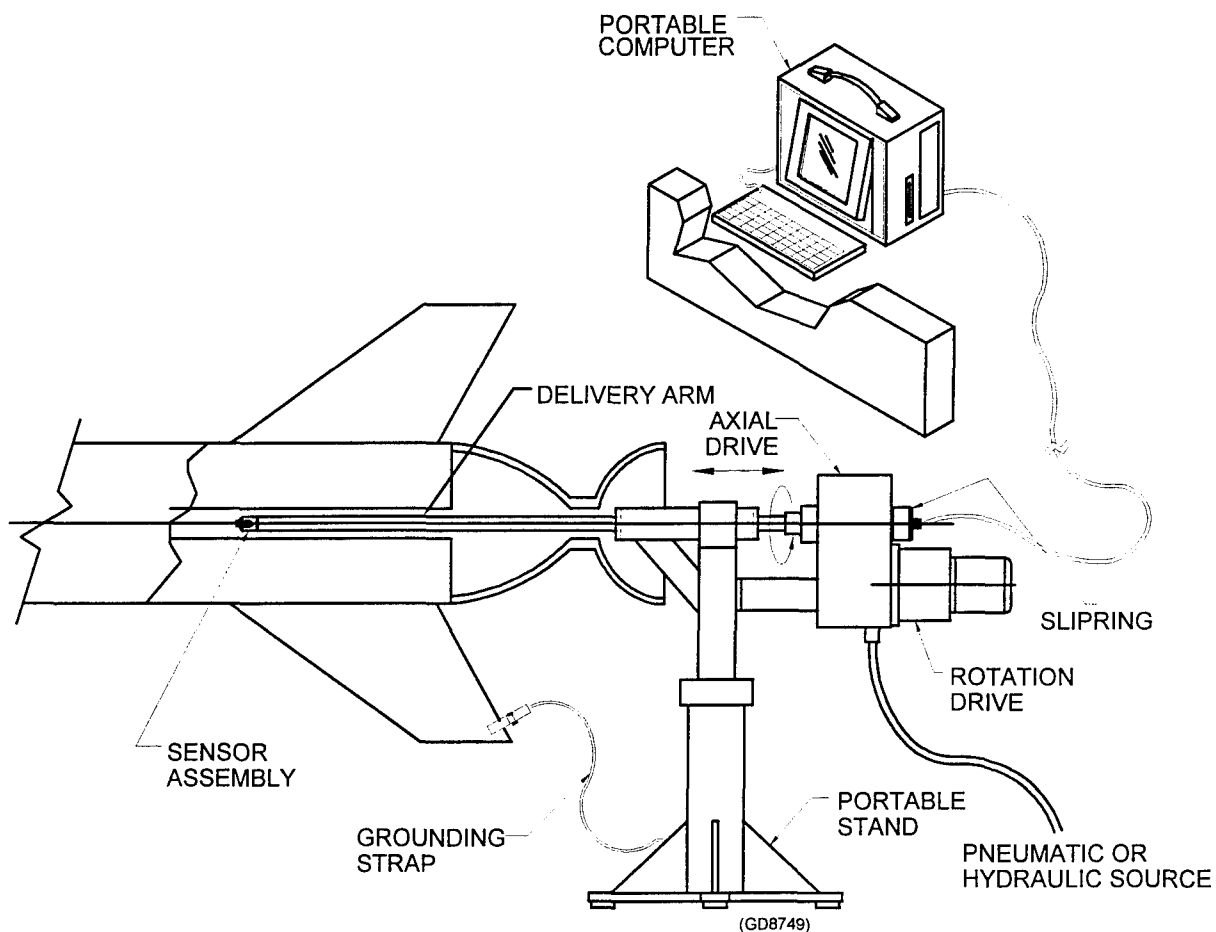


Figure 32. Conceptual view of Solid Rocket Motor Inspection System.

The following is a brief description of each subsystem.

### 5.2.1 Sensor Assembly

The “lead” concept for the sensor configuration is based on previously field-proven methods that have been employed in two of QUEST’s products. The following discussion will address the fiber-optic light source/lateral-effect photodetector (FO/LE) receiver concept. However, if the results of the system specification task indicate that the FO/LE concept is unacceptable, QUEST will revise the sensor design to reflect the requirements. The sensor assembly (Figure 33) will be composed of three primary subassemblies: a light source, a set of receiving optics, and a linear photodetector. No active electronic components will be employed in the probe, which minimizes the potential for electrical spark.

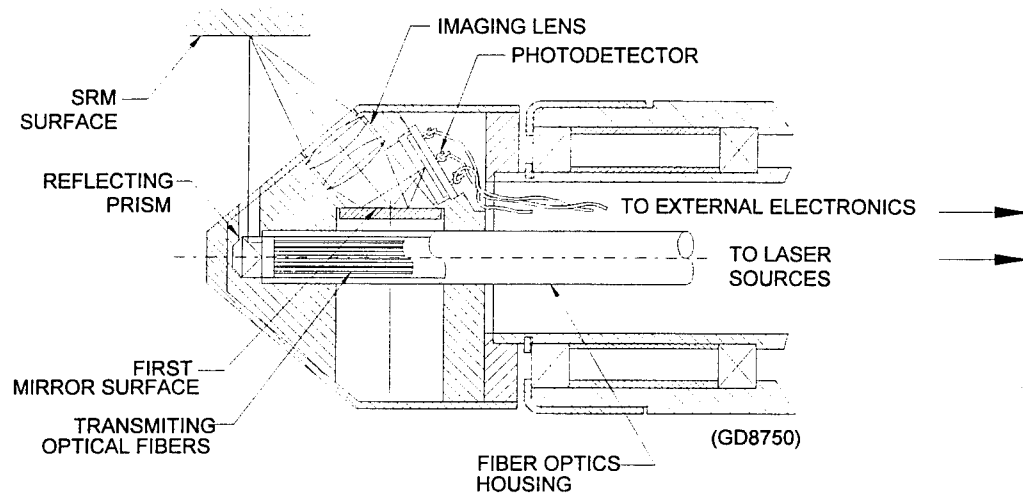


Figure 33. Sensor assembly.

Light Source. To minimize the use of active electronics in the sensor assembly, a fiber-optic laser transmitter will be employed. This assembly will be comprised of an 830-nm infrared diode laser that will be housed external to the rocket motor. For ease of maintenance, the diode laser will be interfaced to a single mode fiber via a detachable connector. The optical fiber will be shielded with a 500-micron buffer to protect it from abrasion. It will be routed through the sensor extension and terminated within the sensor assembly. A gradient index (GrIn) lens will be bonded to the end of the optical fiber and then potted into a protective ferrule, which will provide additional mechanical strength to the lens/fiber joint. The GrIn lens is unique; it provides beam-forming capabilities in an extremely small package. This is possible because the index of refraction of the lens varies linearly as a function of distance from the centerline of the lens. The approximate size of the GrIn lens that we will employ is 0.5 mm in diameter by 2 mm long. Figure 34 shows a photograph of a 0.5-mm-diameter GrIn lens (center of picture) that was

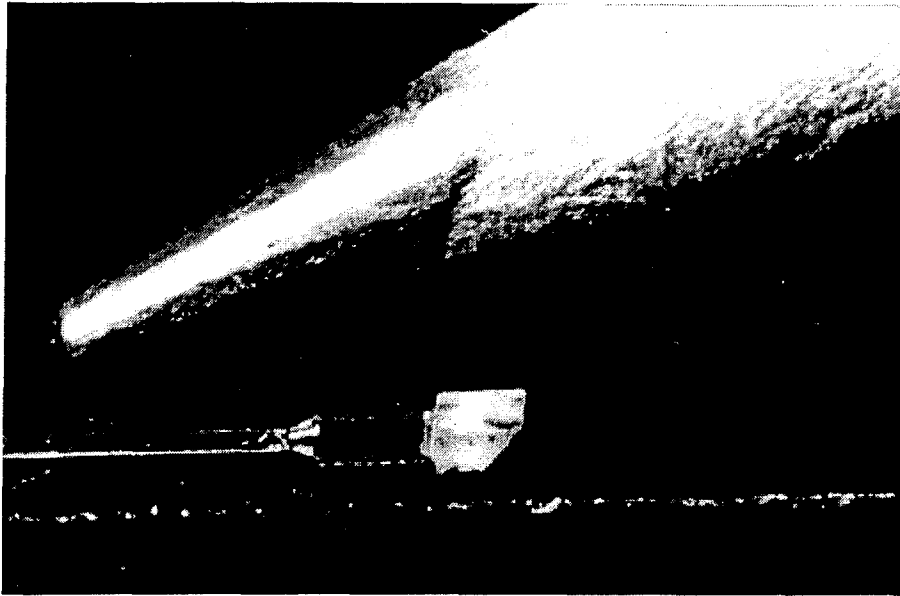


Figure 34. Photo of GrIn lens attached to optical fiber.

attached to a 0.25-mm-diameter optical fiber (left). A small prism (right) is used to reflect the laser light at a 90-degree angle to the probe axis. This assembly was built by QUEST for its Laser-Optic Tube Inspection System (LOTIS™) Model 200 K.

The light that is emitted from the transmitting fiber will be collimated in order to maintain a consistent “footprint” over its measuring range. The diameter of the footprint will be selected as a function of the minimum crack that must be detected. At this point, the diameter is expected to be approximately 0.25 to 0.5 mm. A miniature prism will reflect the light orthogonal to the axis of the sensor and onto the surface of the propellant.

Energy density of the light beam imparted onto the propellant surface is a safety-related issue. As part of the system specification, we will determine the maximum allowable energy density and assure that it cannot be exceeded. The light source will be a low-power (less than 5 mW) pulsed diode laser. The duty cycle will be selected to achieve sufficient return light levels and yet not exceed safety requirements.

Receiving Optics. The reflected signal will be imaged onto the photodetector surface via a set of optics designed to operate over a relatively large range, with a standoff distance of up to several centimeters. QUEST has extensive experience in the design of unique optical systems that can operate under harsh conditions. Computer-based optical design programs, such as Zemax and OPTEC, are used to develop our optical systems and theoretically evaluate their performance before hardware is fabricated.

Detector. The detector will consist of a silicon lateral-effect photodiode coupled through twin transimpedance amplifiers to a pair of 12-bit analog-to-digital converters. The digital signal outputs will be processed by a high-speed digital signal processor (DSP) chip to produce radial profile data.

An example of an automated, laser-based inspection system based on this technology is QUEST's LOTIS, shown in Figure 35. A probe (Figure 36) projects a minute spot of laser light (approximately 0.25 mm in diameter) onto the inside surface of a boiler tube. The sensor rotates at up to 1,800 rpm as it is drawn through the length of a tube (Figure 37). The system generates a helical array of data points that are used to generate a detailed map of the inside surface of the tube. The results are displayed in cross-sectional and isometric perspectives that quantitatively map the inside surface of the tube (Figure 38). In addition, tabular listings of features and dimensions are available.



Figure 35. Laser-Optic Tube Inspection System.

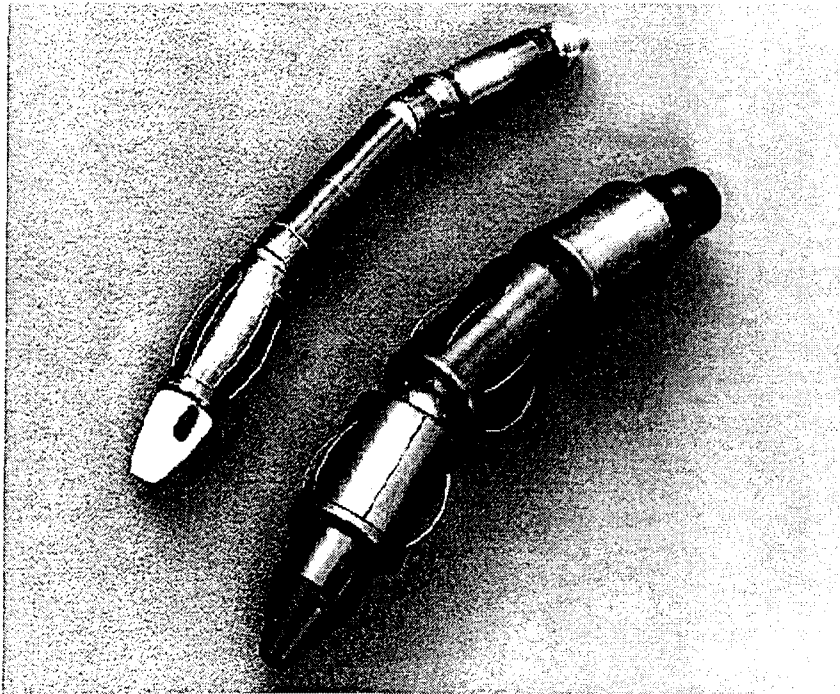


Figure 36. LOTIS probes.

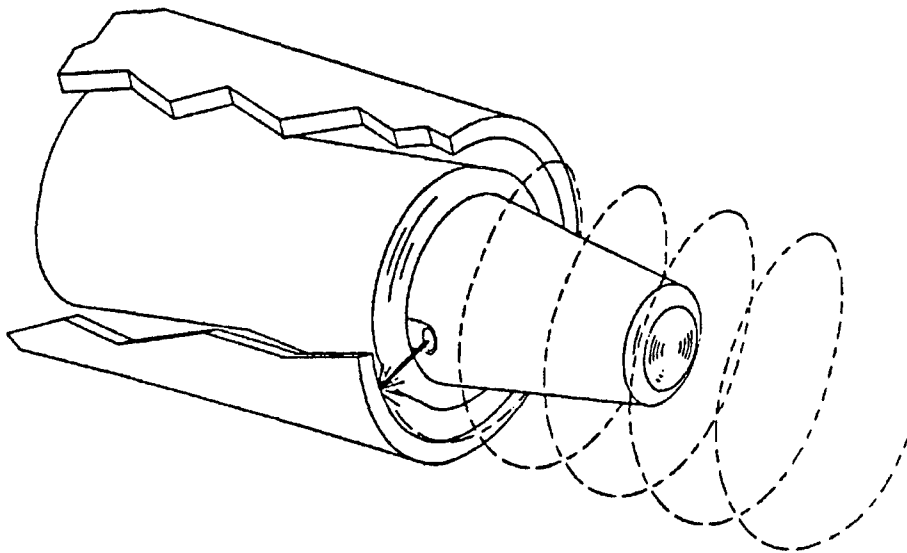


Figure 37. Rotating LOTIS sensor.

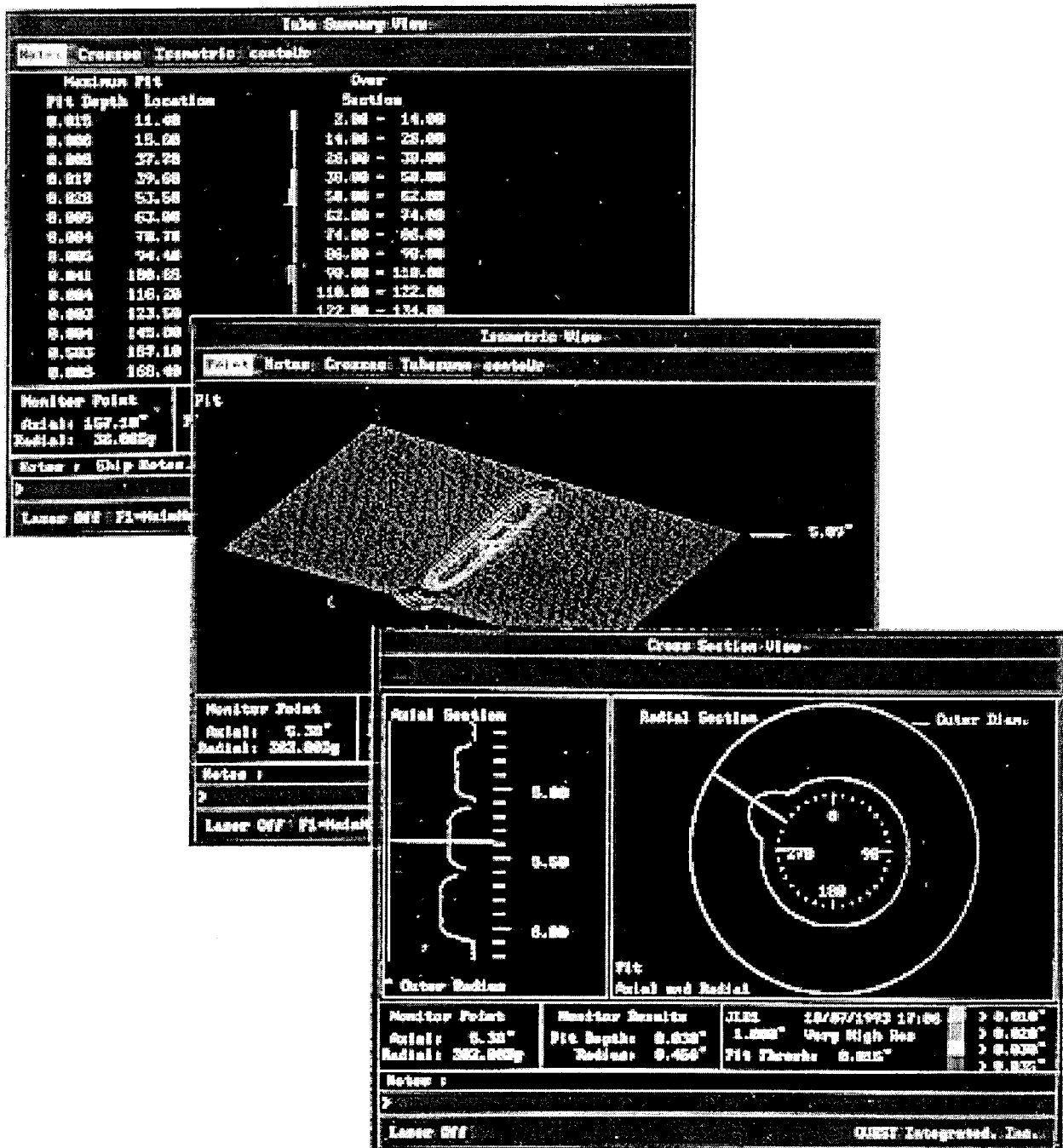


Figure 38. The results of automated laser-based scanning of the inside surface of a tube displayed in summary, isometric, and cross-sectional perspectives.



### 5.2.2 Delivery System

The delivery system will be designed for stability and transportability. Shown in conceptual perspective in Figure 39, the delivery system will provide axial and rotational translation of the sensor assembly and may employ either a pneumatic or hydraulic drive system to minimize the use of potential spark-generating electrical motors. High-resolution linear and angular encoders will provide positional information for surface mapping.

In addition to other safety-related steps, the delivery system may be nitrogen purged to maintain explosion-proof qualification.

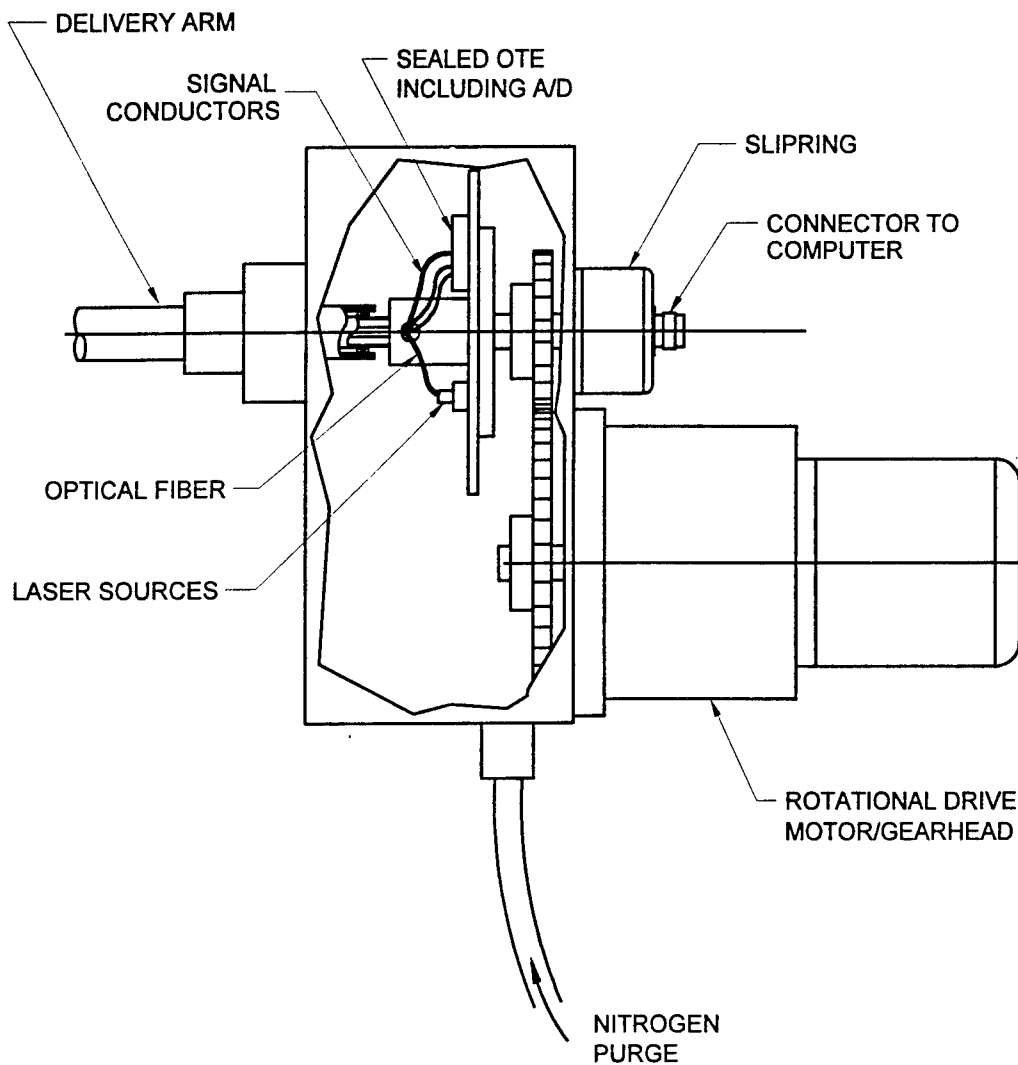


Figure 39. Delivery system.

### 5.2.3 Data Acquisition and Display System

The Data Acquisition and Display System (DADS) will be composed of a field-grade industrial portable computer with extra slots to house the motor control digital signal processing boards. The computer will then postprocess and store the inspection results and act as the operator interface. The system will be provided with an optical storage unit for data archival. Figure 40 shows a functional block diagram of the system.

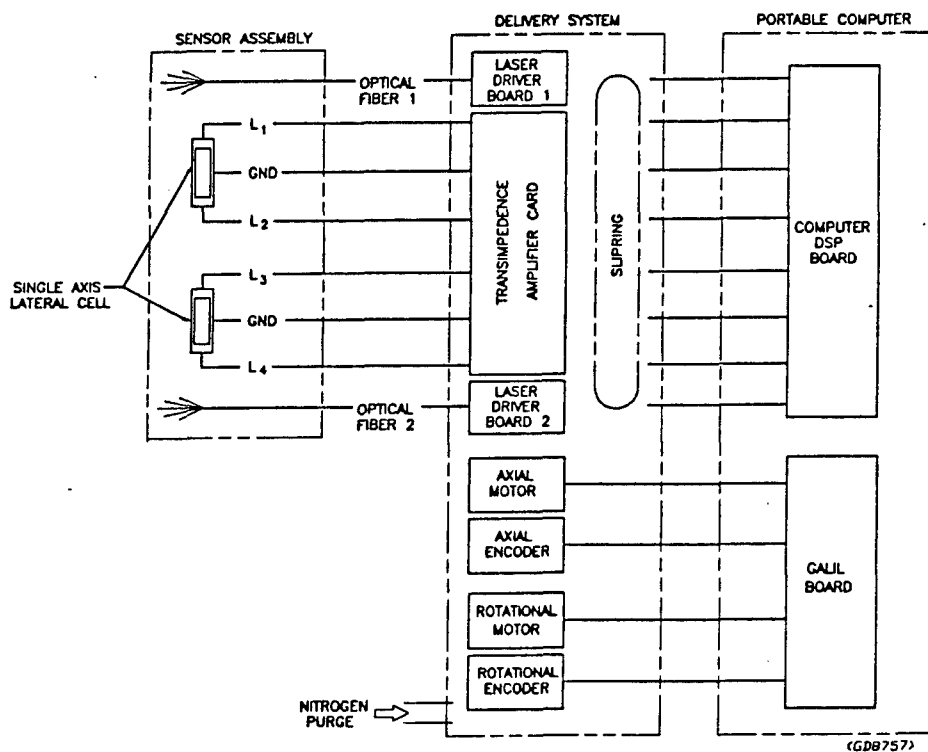


Figure 40. Block diagram of SRMIS Data Acquisition and Display System.

### 5.2.4 Design Review

At the conclusion of the effort, a design review will be held at QUEST headquarters. The sponsor will be invited to attend the technical review meeting and provide any final input prior to fabrication of the prototype SRMIS. Any required design modifications will be implemented prior to fabrication.

### 5.3 SUMMARY OF PHASE I RESULTS

The work on a task-by-task basis conducted under Phase I is summarized as follows:

#### 5.3.1 Task 1 - Select Test Case

On two occasions, meetings were held with the sponsor to discuss all aspects of the program. We agreed upon a test case for the interior surface profile for a relatively difficult “star” cross section of the motor. In addition, QUEST was provided access to an inert solid propellant motor stimulant for a short period of time for evaluation.

#### 5.3.2 Task 2 - Select Optimum Sensor Configuration

The star-shaped geometry of the cross section restricted the allowable optical design geometries to those capable of accessing the entire interior surface. QUEST performed a series of optical measurements to develop a surrogate material to fabricate test specimens. Reflectance measurements were conducted for the sample propellant surrogate provided, and a form of modeling clay was identified as an appropriate material. Two sensors were selected for testing: a commercially available laser triangulation head and a sensor that was designed and built by QUEST. As a result of the laboratory testing, an understanding of the behavior of laser-based triangulation sensors in this application was achieved. Although more work needs to be done in Phase II, a basis for the design has been established.

#### 5.3.3 Task 3 - Build Laboratory Test Setup

A three-axis laboratory robot was modified to accommodate both optical heads designated for these tests. In addition, models of one lobe of the interior star cross section of the solid propellant were constructed out of modeling clay. These models were identical in surface reflectivity and surface roughness to the sample of solid propellant provided. Figure 13 shows the laser triangulation head mounted on the three-axis Cartesian robot. A scan of a defect free section is shown in Figure 17. Note that a single arm was scanned and duplicated assuming hexagonal symmetry. Various types of cracking and slumping flaws were simulated in the modeling clay that was then fired and placed into mounts for scanning. Figure 20 shows a photograph of a sample with a tight crack and a slump.

#### 5.3.4 Task 4 - Conduct Laboratory Tests

Laboratory tests were conducted in which the specified optical head mounted on the robot was used to scan the various models. Results are shown in Figures 5 and 21 for the sample with the crack and slump. The demonstrated accuracy for the selected cross section was a surface measurement accuracy of 0.013 mm or better for the entire range of radii measured. We also attempted to simulate propellant migration by placing small drops of epoxy on the surface. The results from those measurements are shown in Figure 25. Note the presence of five surface defects. We clearly demonstrated the ability to detect small changes in surface reflectivity or surface shape due to the presence of droplets on the surface.

#### 5.3.5 Task 5 - Assimilate Results and Define Conceptual Inspection System

The encouraging results obtained from our laboratory tests have been assimilated and a conceptual inspection system developed. The details of this inspection system are presented in the Phase II technical proposal.

## 6. SUMMARY AND CONCLUSIONS

In summary, we have conducted a preliminary design study for a nondestructive evaluation tool based on optical triangulation for use in the internals of SRM's. The following conclusions can be reached as a result of our study:

1. Optical triangulation has been demonstrated on material with similar optical properties to propellants over the expected dynamic range of radii.
2. Laboratory demonstration has demonstrated the ability of optical triangulation to reliably detect cracking and slumping. In addition, the technique has established a high probability of being capable of detecting changes in surface reflectivity, which may be caused as a result of propellant migration.

In addition to the results of the Phase I study, a summary of a preliminary design to be conducted under Phase II was presented. The design will present some challenges for the design of an all-glass optical head to be safety compliant but should be readily achievable under Phase II.

## 7. RECOMMENDATIONS

Based on the successful results generated under the Phase I feasibility study, QUEST Integrated, Inc., recommends the funding of a Phase II program to develop a full-scale prototype solid rocket motor inspection system. Based on our preliminary indications, there is significant need for such a system within both the Department of Defense and commercial industry. Specific actions that are recommended include:

- Develop a detailed specification for a laser-based Solid Rocket Motor Inspection System (SRMIS).
- Identify a candidate rocket motor that has a history of propellant-related problems and is currently in use by the Department of Defense and other agencies.
- Identify a facility in which to deliver and set up the SRMIS.
- Design, fabricate, and test a full-scale prototype SRMIS.
- Determine the market potential for a commercial version of the SRMIS (Phase III).

APPENDIX  
MATLAB SCRIPTS FOR ANALYSIS AND DISPLAY

```

function [X,Y,Z]= head2nat ( inmat, standoff, mult )
%
% Converts a raw x,w robot raster scan to natural frame of reference. Usage:
%
%   [X,Y,Z]= head2nat ( inmat, standoff, mult )
%
%   where:  inmat is the input matrix n x m
%           standoff is the standoff distance of the measurement head in mm.
%           mult is the factor that converts DAS8 signal to mm
%           X,Y,Z are the natural coordinates.

% definitions
rad2deg= pi/180;

% determine size
rnk= size(inmat)
emax= rnk(1);

% determine TH
thulim= max(inmat(:,2));
thllim= min(inmat(:,2));
thstep= fix(100*(inmat(2,2)-inmat(1,2)+0.005))/100;
TH= thllim:thstep:thulim;
ithmax= size(TH);
ithmax= ithmax(2);

% determine Z
zllim= inmat(1,1);
zulim= inmat(emax,1);
idx= find(inmat(:,1)>inmat(1,1));
zstep= fix(10000*(inmat(idx(1))-inmat(1,1)+0.00005))/10000;
z= zllim:zstep:zulim;
z= z*25.4;
izmax= size(z);
izmax= izmax(2);

% extract Rin (ithmax,izmax) from input array.
Rraw= reshape(inmat(:,3),ithmax,izmax);
% Remove 5 sigma outliers by row (see zrorow.m help)
Rin= zrorow(Rraw,5);

% Convert to mm
Rin= (Rin*mult)+standoff;

% Loop, form arrays;
for i= 1:1:ithmax;
    for j= 1:1:izmax;
        X(i,j)= Rin(i,j) * cos(TH(i)*rad2deg);
        Y(i,j)= Rin(i,j) * sin(TH(i)*rad2deg);
        Z(i,j)= z(j);
    end;
end;

% SEE YA!

```



```

function AccOff= detoff (X, Y, n)
%
% Determines the proper offset in x such that the subtending angle from the
% origin is an angle 360/n. Usage:
%
% offset= detoff ( X, Y, n)
%
% where X, Y are the (x,y) natural coordinates of the part and
% n is the number of points.
rank= size(X)
ilim= rank(1);
jlim= rank(2);

rad2deg= 180/pi;
TargetAngle= 360/n * (1 - 1/ilim)
offset= 10;
Angle= 0;
AccOff= 0;
gt= -1;

% Get positional means
xpl= mean(X(ilim,:));
yp1= mean(Y(ilim,:));
xp2= mean(X(1,:));
yp2= mean(Y(1,:));

Angle= (atan(yp1/xpl) + atan(-yp2/xp2)) * rad2deg;
while (~((Angle<TargetAngle+0.1) & (Angle>TargetAngle-0.1)));
    if (Angle<TargetAngle);
        if (gt==1)
            offset= offset/2;
        end;
        AccOff= AccOff+offset;
        xpli= xpl-AccOff;
        xp2i= xp2-AccOff;
        Angle= (atan(yp1/xpli) + atan(-yp2/xp2i)) * rad2deg;
        gt= 0;
    end;
    if (Angle>TargetAngle);
        if (gt==0)
            offset= offset/2;
        end;
        AccOff= AccOff-offset;
        xpli= xpl-AccOff;
        xp2i= xp2-AccOff;
        Angle= (atan(yp1/xpli) + atan(-yp2/xp2i)) * rad2deg;
        gt= 1;
    end;
end;
end;

```

```

function [R,T]= nat2rt ( X, Y, offset )
%
% Transforms natural coordinates to cylindrical. Output R and T are matrices.
% output may be fed to rtmirror which will reflect the star point around the a
% develop a full rocket scan. X,Y are natural coordiantes, offset is an offse
% that makes the scan subtend a given angle 360/n, where n is the number of st
%
% [R,T]= nat2rt ( X, Y, offset )

rank= size(X)
ilim= rank(1);

X= X-offset;

for i= 1:1:ilim;
    R(i,:)= sqrt ( X(i,:) .^ 2 + Y(i,:) .^ 2 );
    T(i,:)= atan ( Y(i,:) ./ X(i,:) );
end;

```

```

function [RR,TT,ZZ]= rtmirror (R, T, Z, n)
%
% Mirrors a scan about the symmetry axis in order to simulate a full rocket scan
%
% [Rfull Tfull Zfull]= rtmirror ( R, T, Z )
%
% where R, T, Z, are matrices from nat2rt (cylindrical transform)
% n is the number of star points (even).
% Rfull, Tfull, Zfull are the filled rotated matrices.

rank= size(R)
ilim= rank(1);
jlim= rank(2);
subtend= 2*pi/n;

RR= R;
TT= T+subtend/2;
ZZ= Z;

nrefl= 1;

% Reflect one point about axis of symmetry.
for i= 1:1:ilim;
    outcol= ilim+i;
    incol= ilim-i+1;
    RR(outcol,:)= RR(incol,:);
    TT(outcol,:)= 2*subtend - TT(incol,:);
    ZZ(outcol,:)= ZZ(incol,:);
end;
nrefl= 2;

% Reflect two points about upper limit until around.
while (nrefl < n)
    for i= 1:1:2*ilim;
        outcol= nrefl*ilim + i;
        incol= nrefl*ilim - i+1;
        RR(outcol,:)= RR(incol,:);
        TT(outcol,:)= 2*nrefl*subtend - TT(incol,:);
        ZZ(outcol,:)= ZZ(incol,:);
    end;
    nrefl= nrefl+2;
end;

RR(outcol+1,:)= RR(1,:);
TT(outcol+1,:)= TT(1,:);
ZZ(outcol+1,:)= ZZ(1,:);

```

```

function [X,Y]= rt2nat ( R, T )
%
% Transforms cylindrical coordinates to natural. Input R and T are matrices. T
% output may be fed to plotnat, which will grid plot the simulated scan.
% X,Y are natural coordiantes.
%
% [X,Y]= nat2rt ( R, T )

rank= size(R)
ilim= rank(1);

for i= 1:1:ilim;
    X(i,:)= R(i,:) .* cos(T(i,:));
    Y(i,:)= R(i,:) .* sin(T(i,:));
end;

```

```

function [x, y, z, X, Y, Z]= trans ( dataset, standoff, mult, n )
%
% Transforms a rocket data set into natural coordinates and reflected pseudo-sca
% coordinates. Usage:
%
% [x, y, z, X, Y, Z]= trans ( dataset, standoff, mult, n )
%
% where dataset is the raw data set from the robot computer
% standoff is the standoff distance in mm
% mult is the multiplication factor to turn DAS8 units to mm
% n is the number of points on the star
% x,y,z are natural coordinates
% X,Y,Z are reflected natural coordinates

[x y z]= head2nat(dataset,standoff,mult);
offset= detoff(x,y,n);
[r t]= nat2rt(x,y,offset);
[R T Z]= rtmirror(r,t,z,n);
[X Y]= rt2nat(R,T);
mesh(X,Y,Z);

```

## DISTRIBUTION LIST

AUL/LSE Bldg 1405 - 600 Chennault Circle Maxwell AFB, AL 36112-6424	1 cy
DTIC/OCP 8725 John J. Kingman Rd, Suite 0944 Ft Belvoir, VA 22060-6218	2 cys
AFSAA/SAI 1580 Air Force Pentagon Washington, DC 20330-1580	1 cy
PL/SUL Kirtland AFB, NM 87117-5776	2 cys
PL/HO Kirtland AFB, NM 87117-5776	1 cy
Official Record Copy PL/VT-B/Sandra Slivinsky Kirtland AFB, NM 87117-5776	2 cys
PL/VT Dr Wick Kirtland AFB, NM 87117-5776	1 cy